



LAWRENCE  
LIVERMORE  
NATIONAL  
LABORATORY

# Experimental characterization of initial conditions and spatio-temporal evolution of a small Atwood number Rayleigh-Taylor mixing layer

N. J. Mueschke, M. J. Andrews, O. Schilling

September 29, 2005

Journal of Fluid Mechanics

This document was prepared as an account of work sponsored by an agency of the United States Government. Neither the United States Government nor the University of California nor any of their employees, makes any warranty, express or implied, or assumes any legal liability or responsibility for the accuracy, completeness, or usefulness of any information, apparatus, product, or process disclosed, or represents that its use would not infringe privately owned rights. Reference herein to any specific commercial product, process, or service by trade name, trademark, manufacturer, or otherwise, does not necessarily constitute or imply its endorsement, recommendation, or favoring by the United States Government or the University of California. The views and opinions of authors expressed herein do not necessarily state or reflect those of the United States Government or the University of California, and shall not be used for advertising or product endorsement purposes.

**Experimental characterization of initial conditions and spatio-temporal evolution of a  
small Atwood number Rayleigh-Taylor mixing layer**

Nicholas J. Mueschke<sup>1</sup>, Malcolm J. Andrews<sup>1</sup> & Oleg Schilling<sup>2</sup>

1) Department of Mechanical Engineering

Texas A&M University

College Station, TX 77843

2) University of California

Lawrence Livermore National Laboratory

Livermore, CA 94550

Submitted to:	Journal of Fluid Mechanics
Date Submitted:	xx/xx/xx
Type of paper:	Full-length article
Address of correspondence:	Professor Malcolm J. Andrews Dept. of Mechanical Engineering Texas A&M University College Station, TX 77843-3123 Tel: (979) 847-8843 Fax: (979) 845-3081 Email: mandrews@tamu.edu

**Experimental characterization of initial conditions and spatio-temporal evolution of a  
small Atwood number Rayleigh-Taylor mixing layer**

Nicholas J. Mueschke, Malcolm J. Andrews & Oleg Schilling

**Abstract**

The initial multi-mode interfacial velocity and density perturbations present at the onset of a small Atwood number, incompressible, miscible, Rayleigh-Taylor instability-driven mixing layer have been quantified using a combination of experimental techniques. The streamwise interfacial and spanwise interfacial perturbations were measured using high-resolution thermocouples and planar laser-induced fluorescence (PLIF), respectively. The initial multi-mode streamwise velocity perturbations at the two-fluid density interface were measured using particle-image velocimetry (PIV). It was found that the measured initial conditions describe an initially anisotropic state, in which the perturbations in the streamwise and spanwise directions are independent of one another. The evolution of various fluctuating velocity and density statistics, together with velocity and density variance spectra, were measured using PIV and high-resolution thermocouple data. The evolution of the velocity and density statistics is used to investigate the early-time evolution and the onset of strongly-nonlinear, transitional dynamics within the mixing layer. The early-time evolution of the density and vertical velocity variance spectra indicate that velocity fluctuations are the dominant mechanism driving the instability development. The implications of the present experimental measurements on the initialization of Reynolds-averaged turbulent transport and mixing models and of direct and large-eddy simulations of Rayleigh-Taylor instability-induced turbulence are discussed.

## 1. Introduction

A complete understanding of the transitional dynamics in instability-driven turbulent flows remains a fundamental challenge for turbulence theory and modeling. Canonical two-fluid hydrodynamic instabilities, such as the Kelvin-Helmholtz, Rayleigh-Taylor, and Richtmyer-Meshkov instabilities, develop from a quiescent or laminar state, become transitional, and eventually fully-developed. While the linear and weakly non-linear theories for the growth of these shear- and buoyancy-driven instabilities are well developed (Chandrasekhar 1961; Brouillette 2002; Drazin & Reid 2004), the transitional dynamics of such instability driven flows and their fully-turbulent state are not as well defined. Transitional flows are difficult to treat analytically as they possess many of the same chaotic properties of fully-developed turbulent flows (Drazin 2002; Criminale, Jackson & Joslin 2003) including spatio-temporal evolution, inhomogeneity and anisotropy, intermittency of the transitional and free-stream flow and, in the case of interfacial hydrodynamic instabilities in which two or more fluids are present, species transport and molecular mixing. Further complications arise due to the relatively poorly understood dependence of the transitional and turbulent flow generated by interfacial instabilities on the initial conditions (Husain & Hussain 1979; Dalziel, Linden & Youngs 1999; Mi, Nobes & Nathan 2001; Cook & Dimotakis 2001; Faisst & Eckhardt 2004; Ramaprabhu, Dimonte & Andrews 2005). An objective of the present work is to examine the evolution of a transitional flow induced by the Rayleigh-Taylor instability in detail as it approaches a fully-developed turbulent state using state-of-the-art experimental diagnostics.

The transitional stage between the early-time growth of perturbations and fully-developed turbulence has been experimentally studied in a variety of fluid configurations. Studies of transitional flows date back to the examination of the onset of turbulence in pipe flows (Reynolds 1883). A more recent experimental study of the transitional regime in pipe flows by Darbyshire and Mullin (1995) examined this regime using sophisticated diagnostics and controlled perturbations. Measurements of the initial conditions and the characterization of the transition to turbulence in planar shear layers have received considerable attention (Bradshaw 1966; Brown & Roshko 1974; Bell & Mehta 1993; Weygandt & Mehta 1995). Recently, Marmottant and Villermaux (2004) examined the initial perturbations of a liquid to investigate the growth of Kelvin-Helmholtz and Rayleigh-Taylor instabilities as the liquid jet transitioned to an atomized spray. Measurements of the initial conditions and of the transition stages in shear layer flows have been well studied; however, the experimental characterization of the

initial conditions and transition regime in buoyancy-driven turbulent mixing layers remains quite limited. Measurements of the initial, multi-mode perturbations of interfacial instabilities have proven to be non-trivial, as evidenced by the paucity of experimental results in this area. The magnitudes of the interfacial position and velocity fluctuations are typically very small, and thus difficult to resolve experimentally in non-stationary flows. Dalziel, Linden and Youngs (1999) measured the velocity field generated by the removal of a thin barrier initially separating two fluids of different densities which then interpenetrated and evolved into a turbulent mixing layer. Milovich *et al.* (2004) and Dimonte (2004) have reported measurements of initial perturbations on the exterior shell of an inertial confinement fusion (ICF) target. The goal of the present work is to completely and accurately quantify the perturbations present at the onset of a buoyancy-driven Rayleigh-Taylor mixing layer and to examine the development of the characteristics of a transitional mixing layer.

In addition, the complex dynamics that arise as a flow begins to develop characteristics of fully-developed turbulence present several issues for the development of turbulent transport and mixing [Reynolds-averaged Navier-Stokes (RANS)] models in the transitional regime. Modeling complex, multi-scale, variable-density turbulent flows characterized by an expanding range of timescales and lengthscales continues to represent a grand challenge for the turbulence community. The validation of predictive turbulent transport models of anisotropic, inhomogeneous, variable-density turbulence and mixing requires *a priori* knowledge of second- and higher-order correlations of velocity and density fluctuations, such as  $\overline{\rho'^2}$ ,  $\overline{u'_i u'_j}$ ,  $\overline{\rho' u'_j}$  and  $\overline{u'_i u'^2 / 2 + p' u'_i}$ , where the overbar denotes Reynolds averaging. Turbulent mixing layers induced by the Rayleigh-Taylor instability represent a special case in which the flow is initially quiescent or laminar, becomes transitional, and finally turbulent. Currently, the proper initialization of quantities required in turbulent transport models, such as the turbulent kinetic energy and its dissipation rate, or the coupling of the initial conditions to subgrid-scale models for large-eddy simulations (LES), is an open research topic in Rayleigh-Taylor instability-driven mixing. Thus, this work is partly motivated by the need for detailed experimental data to assess and to further develop both RANS and subgrid-scale models that include the effects of initial conditions on Rayleigh-Taylor instability-induced mixing.

To accomplish the principal objective of this investigation, the initial interfacial and velocity perturbations at the two-fluid interface of a small Atwood number Rayleigh-Taylor mixing layer were experimentally measured in a water channel facility at Texas A&M University. Also, the measured time-evolution of various velocity, density,

mixing statistics and spectra is presented to further elucidate the role of initial conditions in the early-time development of a Rayleigh-Taylor instability-driven mixing layer. Details on the experimental facility are provided in § 3 and the experimental results are reported in § 4. Hence, the present work provides detailed experimental measurements of the initial conditions and the early-time development of a buoyancy-driven mixing layer.

## 2. Previous experimental investigations of Rayleigh-Taylor instability and mixing

The Rayleigh-Taylor instability occurs when a heavy fluid with density  $\rho_1$  is accelerated towards a lighter fluid with density  $\rho_2$  and the fluid layers are initially separated by a perturbed interface (Rayleigh 1884; Taylor 1950). For the case considered here, the acceleration is that of Earth's gravity  $g = 981 \text{ cm/s}^2$ . A Rayleigh-Taylor unstable stratification exists when the density and pressure gradients are oriented such that  $\nabla \rho \cdot \nabla p < 0$ . With small-amplitude perturbations at the two-fluid interface, each mode grows exponentially and independently at early times according to linear theory (Chandrasekhar 1961; Drazin & Reid 2004) until nonlinear modal interactions ensue (Sharp 1984; Haan 1989) and smaller modes merge to create larger buoyant structures: bubbles of lighter fluid “rise” in the direction opposite to the acceleration, while spikes of heavier fluid “fall” in the direction of the acceleration. Secondary Kelvin-Helmholtz instabilities grow as localized regions of high shear develop between the rising bubbles and the falling spikes (Sharp 1984). As the amplitude of a particular mode approaches half of its wavelength, the growth rate of that mode *saturates* (Youngs 1984). Finally, as the mixing layer becomes turbulent and grows in spatial extent, dimensional analysis shows that (in the absence of dissipative, diffusive, surface tension and other effects) the only relevant dynamical lengthscale is  $gt^2$ . In this late-time self-similar regime, the appropriately defined penetration of the bubble front in a mixing layer scales quadratically in time as

$$h_b(t) = \alpha A g t^2, \quad (1)$$

where  $A \equiv (\rho_1 - \rho_2)/(\rho_1 + \rho_2) > 0$  is the Atwood number and  $\alpha$  is a dimensionless function of the Atwood number, Reynolds number, and possibly other parameters (Anuchina *et al.* 1978; Youngs 1984; Cook & Dimotakis 2001). In the limit of very small Atwood number, as considered in the present work,  $h_b$  is approximately equal to the penetration of the spike front  $h_s$ . The determination of the exact conditions under which the self-similarity implied by Eq. (1) is satisfied is currently an active area of investigation (Cook & Dimotakis 2001; Dimonte *et al.* 2004;

Ramaprabhu & Andrews 2004b; Cook, Cabot & Miller 2004; Dimonte *et al.* 2005) and is not further considered in the present work.

The focus of experiments and the sophistication of diagnostics employed in Rayleigh-Taylor mixing experiments have evolved considerably over the past fifty years, as briefly reviewed below. Initial studies examined two-dimensional, single-mode Rayleigh-Taylor instabilities using purely optical techniques, while more recent research has focused on the examination of the internal, turbulent structure and initial conditions of multi-mode Rayleigh-Taylor mixing layers using sophisticated flow diagnostics. Early experiments by Allred, Blount and Miller (1954) used optical techniques to examine the development of Rayleigh-Taylor perturbations on a rising bubble front. Emmons, Chang and Watson (1960) pioneered the method of accelerating a tank containing two fluids of different densities, thereby creating a Rayleigh-Taylor unstable interface. They obtained an approximate single-mode perturbation at the density interface by oscillating a paddle and restricted their experiments to the simpler, single-mode case. The growth of individual bubbles and spikes was measured using high-speed photography. Other researchers have also used some type of accelerated tank containing miscible or immiscible fluids of different densities to investigate the growth of Rayleigh-Taylor instability-driven mixing layers (Ratafia 1973; Cole & Tankin 1973; Popil & Curzon 1979; Read 1984; Jacobs & Catton 1988; Kucherenko *et al.* 1994, 1997, 2003a,b; Dimonte & Schneider 1996, Dimonte 1999; Wilkinson 2004). Some experiments imposed an approximate sinusoidal perturbation at the two-fluid interface and primarily used optical techniques to measure the growth of individual structures (bubbles and spikes) (Ratafia 1973; Cole 1973; Popil & Curzon 1979; Jacobs 1988; Wilkinson 2004). In addition to the measurement of the mixing layer width, Wilkinson (2004) used planar laser-induced fluorescence (PLIF) to measure the growth and internal structure of the single-mode, three-dimensional Rayleigh-Taylor instability. Other researchers have either allowed ambient noise or intentionally-created initial, multi-mode perturbations to seed the instability (Read 1984; Dimonte & Schneider 1996; Dimonte 1999; Kucherenko *et al.* 1997, 2003a,b). In this multi-mode case, optical techniques were used to measure the growth of the turbulent mixing layer, rather than the amplitudes of individual bubbles and spikes. Standard photographic techniques limited investigations to the quantification of the spatial growth of the mixing layer; measurements of the internal structure of the mixing layer, and the quantification of the degree of molecular mixing were not possible. An alternative to using standard photography is to measure mixing layer widths using x-ray radiography (Kucherenko *et*



*al.* 1997, 2003a). Kucherenko *et al.* (2003a) measured the growth of a miscible, turbulent Rayleigh-Taylor mixing layer for different sets of initial diffusion layer thicknesses and small-scale random perturbations. Also, Kucherenko *et al.* (2003b) used laser-induced fluorescence (LIF) to measure the distribution of fluid fragment sizes within an immiscible, Rayleigh-Taylor turbulent mixing layer.

To avoid difficulties associated with the imaging of a flow in an accelerating tank, various researchers have designed Rayleigh-Taylor experiments that were stationary in space. In one such experiment, a tank containing two fluids of different densities was rapidly overturned (Andrews 1986; Andrews & Spalding 1990). These experiments included adverse stratifications of fluids with nominally flat and tilted interfaces. The initial tilt angle of the two-fluid interface and growth of the Rayleigh-Taylor instability-driven mixing layer could be accurately measured using optical techniques, but the initial small-scale perturbations could not be measured. In addition, no detailed data on the internal structure of the mixing layer was obtained. Another approach produced an unstable interface by withdrawing a plate from a tank that separated a heavier fluid situated above a lighter fluid (Linden & Redondo 1991; Linden, Redondo & Youngs 1994; Dalziel, Linden & Youngs 1999). These experiments also used optical techniques to measure the growth of the mixing layer and the average volume fraction profiles across the mixing layer, and also partially quantified the initial conditions. Densitometry was used to measure the degree of molecular mixing as a function of time. In addition, Dalziel, Linden and Youngs (1999) used a particle-tracking method to measure the velocity perturbations in a vertical plane introduced by the horizontal withdrawal of the splitter plate.

Another method for generating a Rayleigh-Taylor unstable interface (and the one used in this work) was pioneered by Snider and Andrews (1994), in which two different water streams (cold and hot) are initially separated by a thin splitter plate. After termination at the knife edge of the splitter plate, the resulting flow configuration is Rayleigh-Taylor unstable and a mixing layer develops downstream. The water channel of Snider and Andrews (1994) was used in the current investigation, and is discussed in detail in § 3. Optical techniques were used to measure the self-similar quadratic-in-time growth of the mixing layer and the average volume fraction (non-dimensional density) profiles across the mixing layer. High-resolution thermocouples and particle-image velocimetry (PIV) were used to investigate the velocity and density fluctuations within the mixing layer, the average volume fraction profiles across the layer, and the degree of molecular mixing within the layer (Wilson & Andrews 2002; Wilson 2002; Ramaprabhu 2003; Ramaprabhu & Andrews 2004a). Density and velocity variance (energy)

spectra were also reported. PIV was also used to measure the components of the Reynolds stress tensor  $\langle u'^2 \rangle$ ,  $\langle w'^2 \rangle$ , and  $\langle u'w' \rangle$  at various downstream locations (Wilson 2002; Ramaprabhu 2003; Ramaprabhu & Andrews 2004a), where  $u$  and  $w$  are the streamwise and vertical velocity components, respectively,  $u' = u - \langle u \rangle$  and  $w' = w - \langle w \rangle$  are the corresponding fluctuating components, and the angle brackets denote a spatial average [see Eq. (5)]. The same water channel configuration was used to measure both large-scale and small-scale statistics (Ramaprabhu 2003; Ramaprabhu & Andrews 2004a), such as the components of the Reynolds stress anisotropy tensor  $b_{ij} \equiv \langle u'_i u'_j \rangle / \langle u'^2 \rangle - \delta_{ij} / 3$  (Pope 2000) where  $\delta_{ij}$  is the Kronecker tensor. The PIV-S (scalar) technique was used to simultaneously measure two-dimensional density and velocity fields, yielding measurements of the density-velocity correlations  $\langle \rho' u' \rangle$  and  $\langle \rho' w' \rangle$  (Ramaprabhu & Andrews 2003) and the balance between potential energy, kinetic energy, and dissipation. In addition to quantifying turbulence statistics, measurements were performed to determine the initial density and velocity fluctuations at the two-fluid interface in the streamwise direction (Ramaprabhu & Andrews 2004a,b). The current investigation provides additional quantitative data on the initial development of a Rayleigh-Taylor mixing layer using a combination of diagnostics, including thermocouples, particle-image velocimetry, and planar laser-induced fluorescence, and will be discussed in § 4.

### 3. Experimental configuration

The water channel is an open-loop facility in which cold water and warm water (at a temperature difference  $\Delta T \approx 5^\circ\text{C}$ ), initially separated by a 3.2 mm thick Plexiglas splitter plate, enter the channel horizontally. A schematic of the water channel, diagnostics, and reference axes are shown in Fig. 1. A density difference between the two streams is induced by thermal expansion of the warmer water. The water channel is supplied from two 500 gallon water tanks; a typical experiment has a running time of approximately ten minutes. Sump pumps in each tank ensure adequate stirring of the water to maintain temperature uniformity. Cold and hot water are pumped into the entrance plenum and each stream flows through an arrangement of flow-straighteners, followed by a series of screen meshes ( $30 \times 30$  wires/in). The screen meshes reduce the free-stream velocity fluctuations, and reduce the momentum deficit caused by boundary layers along the walls of the channel and splitter plate. The splitter plate terminates at a  $2.5^\circ$  knife-edge followed immediately by another screen mesh ( $35 \times 35$  wires/in). This final screen mesh

(end-screen) minimizes the momentum deficit at the end of the splitter plate, thereby reducing the magnitude and wavelength of the wake shed from the splitter plate (Koop 1976; Browand & Weidman 1976; Stillinger *et al.* 1983).

Upon entering the mixing section of the channel, an adverse density stratification exists between the two water streams and a Rayleigh-Taylor instability-driven mixing layer forms downstream. The mixing section is 100 cm long ( $x$ -direction) with cross-sectional dimensions of 20 cm  $\times$  32 cm (width  $\times$  height). In the present experiments, the mean advection velocity is  $U_m \approx 4.75$  cm/s, with the two stream velocities matched so that there is no shear due to mean velocity gradients. The sidewalls have been shown to have negligible influence on the growth rate of the mixing layer (Snider & Andrews 1994). Water channel measurements have also been shown to be statistically-stationary for higher-order moments of velocity and density fluctuations (Wilson 2002; Ramaprabhu 2003).

To illustrate the spatial and temporal mixing layer development within the water channel, an image of the mixing layer is shown in Fig. 2. Nigrosene dye (6.0 g) was added to the top stream for visualization purposes. Small interfacial perturbations, which are sub-pixel in size in Fig. 2, grow and interact to form the mixing layer seen on the right-hand side of the image. The downstream distance is converted to time  $t = x/U_m$  using Taylor's hypothesis, where  $x$  is the downstream position from the trailing edge of the splitter plate (Taylor 1938; Pope 2000). Time is normalized by the characteristic buoyancy timescale (Snider & Andrews 1994; Dalziel, Linden & Youngs 1999; Ramaprabhu & Andrews 2004a)

$$\tau \equiv t \sqrt{\frac{Ag}{H}} = \frac{x}{U_m} \sqrt{\frac{Ag}{H}}, \quad (2)$$

where  $H = 32$  cm is the total height of the mixing layer channel. A summary of the experimental parameters is given in Table 1.

The primary objective of the current investigation is to measure the initial velocity and interfacial perturbations, and to determine their influence on the development of the mixing layer. To accomplish this, three separate and independent measurements were performed to quantify the initial conditions of the flow. Two different techniques were required to measure the initial density or interfacial perturbation in the streamwise ( $x$ ) and spanwise ( $y$ ) direction. A third technique was required to measure the initial velocity fluctuations. First, the *fluctuating density field* shed from the trailing-edge of the splitter plate was inferred from temperatures measured using a

high-resolution thermocouple. Second, *velocity perturbations in the streamwise direction* were measured using particle-image velocimetry (PIV). Third, *interfacial perturbations in the spanwise direction* were measured using planar laser-induced fluorescence (PLIF). In addition to quantifying the initial conditions, the evolution of the fluctuating velocity and density, as well as mixing statistics have been measured to study the transition from weakly-nonlinear to strongly-nonlinear mixing. Details of each experimental method and of the corresponding measurements are given in the next section.

## 4. Experimental measurements

### 4.1. Thermocouple diagnostics and measurements of the streamwise interfacial perturbation

#### 4.1.1. Thermocouple measurements and data acquisition system

The measurement of the density perturbation in the streamwise ( $x$ ) direction was performed using a high-resolution thermocouple temperature measurement system. Temperature fluctuations were measured using E-type thermocouples positioned at multiple downstream locations from the splitter plate, as listed in Table 2. The thermocouples were constructed from 40 gauge wire (0.08 mm diameter) with a weld bead diameter of 0.16 mm—a smaller weld bead diameter than used by previous researchers in this water channel (Snider & Andrews 1994; Ramaprabhu & Andrews 2004a), resulting in a less intrusive diagnostic and improved spatial resolution. Mueschke and Andrews (2005) showed that these spatial resolution enhancements reduced the uncertainty in the mixing statistics and scalar fluctuation spectra. The thermocouple wire, extension wire, and all connections were shielded and grounded to minimize external electromagnetic and radio frequency noise. Temperature measurements were recorded at a rate of 50 kHz using a 16-bit data acquisition system. Spurious noise from the temperature trace was eliminated using a 50-point averaging window, thus reducing the sampling rate to 1 kHz. Using Taylor's hypothesis, at this sampling rate and a mean advection velocity of  $U_m \approx 4.75$  cm/s, each pointwise temperature measurement was separated by 0.048 mm, which is approximately 30% of the diameter of the probe volume. Fluctuations of the temperature measurements at the Nyquist frequency (500 Hz) were found to be below the level of system noise, obviating the need for a more complex filtering algorithm that retains spectral resolution. Temperature measurements were converted to density values using the equation of state of water

$$\rho(T) = \frac{999.8396 + 18.2249 T - 0.007922 T^2 - 55.448 \times 10^{-6} T^3 + 149.756 \times 10^{-9} T^4 - 393.295 \times 10^{-12} T^5}{1 + 18.159 \times 10^{-3} T} \quad (3)$$

in units of  $\text{kg/m}^3$  (Kukulka 1981). Hereafter, density and temperature are used interchangeably, as they are related by Eq. (3).

Three measurements were performed to ensure an accurate measurement of the non-dimensional time  $\tau$ , as  $x$ ,  $U_m$ , and  $A$  are parameters that can vary from one experiment to another and must be measured accurately to determine  $\tau$ . First, the distance between the splitter plate and the probe volume was carefully measured. Second, the Atwood number was accurately measured using a digital temperature probe with a K-type thermocouple to measure the water temperature in each 500 gallon tank. Finally, the mean flow velocity in the water channel was accurately measured using the following procedure. First, the mean advection velocity of both streams was adjusted until no shear was present and  $U_m \approx 4.5\text{--}5.0$  cm/s. The presence of a mean velocity gradient between the two streams was determined by injecting dye on the splitter plate just before the end-screen. Once the dye was entrained into the mixing layer, the “lean” of developing Rayleigh-Taylor bubbles with respect to the vertical ( $z$ ) axis was examined at downstream locations. In the absence of any “leaning”, the difference between the top and bottom stream velocities was shown to be at most  $|U_1 - U_2| < 0.2$  cm/s or  $\sim 5\%$  of the mean advection velocity (Ramaprabhu 2003). To measure  $U_m$ , a syringe was used to inject fluid containing a high concentration of Nigrosene dye. The time  $t_m$  required for a blob of dye to travel a distance  $L_m$  from the end-screen to a marked downstream location was recorded, so that  $U_m = L_m / t_m$ .

#### 4.1.2 Determination of the density

To measure the density values, a thermocouple was mounted on a thin vertical rake that allowed fine adjustment of the probe location in the vertical ( $z$ ) direction. All measurements in the present study were performed at the centerplane of the mixing layer ( $z = 0$ ), defined as the plane at which equal average volume fractions of hot and cold water exist, i.e., the centerplane corresponds to the position at which the average volume fraction of fluid 1 is  $\langle f_1 \rangle = 1/2$ , where

$$f_1 \equiv \frac{\rho(x) - \rho_2}{\rho_1 - \rho_2} \quad (4)$$

is the volume fraction of fluid 1, and the spatial (Reynolds) average of a scalar quantity  $\phi(x, \tau)$  is defined as

$$\langle \phi \rangle(\tau) = \frac{1}{L} \int_0^L \phi(x, \tau) dx . \quad (5)$$

Spatial averaging of pointwise measurements utilizes Taylor's hypothesis such that  $x = U_m t$ ,  $L \equiv U_m N_{samp} / f_{samp}$  is the distance (cm) over which  $\phi(x, \tau)$  was measured,  $N_{samp}$  is the number of samples, and  $f_{samp}$  is the sampling rate (Hz).

It was concluded that a visual inspection of the thermocouple probe placement could not provide an accurate measure of the mixing layer centerline with respect to Eq. (5). Consequently, the following procedure was used to accurately position the probe: a set of temperature measurements was recorded at 200 Hz and  $\langle f_1 \rangle$  was evaluated; depending upon the value of  $\langle f_1 \rangle$ , the position of the probe was adjusted vertically until  $\langle f_1 \rangle = 0.50 \pm 0.025$ ; once the probe was located at the centerplane, data collection commenced with a two minute interval of temperature measurements recorded at 50 kHz. A two minute collection period corresponds to the passage of approximately eighty large-scale (long-wavelength) plumes, ensuring statistical convergence (Wilson & Andrews 2002; Ramaprabhu & Andrews 2004a).

#### **4.1.3. Evolution of the probability distribution function, variance, and kurtosis of volume fraction fluctuations**

The initial density fluctuations were measured by positioning the thermocouple at a distance  $x = 0.5$  cm downstream from the splitter plate. In addition to measurements at  $x = 0.5$  cm, density measurements were also taken at multiple downstream locations at the centerplane of the mixing layer (see Table 2) to investigate the evolution of density statistics. The density statistics of interest include the probability distribution function (PDF), the variance, and the kurtosis of volume fraction fluctuations at various stages of the instability development. In addition, the time-evolution of the density variance spectrum and molecular mixing fraction  $\theta$  (defined below) were also examined.

The PDF of the scalar trace  $\phi$  is defined discretely by

$$P(\phi) = \frac{F(\phi)}{N_{samp} \Delta\phi} , \quad (6)$$

where  $F(\phi)$  is the discrete frequency distribution (histogram) of the scalar  $\phi$ ,  $N_{samp}$  is the number of samples, and  $\Delta\phi$  is the bin width of  $F(\phi)$ . The variance and kurtosis (second- and fourth-order moments) of an ensemble of

scalar measurements are

$$\sigma_\phi^2 = \langle \phi'^2 \rangle, \quad K_\phi = \frac{\langle \phi'^4 \rangle}{\langle \phi'^2 \rangle^2}, \quad (7)$$

respectively, where  $\phi(x)' = \phi(x) - \langle \phi \rangle$  is the scalar fluctuation trace. The variance of the volume fraction fluctuations is a measure of the spread of volume fraction values away from the mean value  $\langle f_1 \rangle = 0.5$ , while the kurtosis is a measure of the sharpness of the volume fraction PDF. Kurtosis values of  $K_{f_1} < 1.8$  indicate a bimodal distribution with peaks at  $f_1 = 0$  and  $f_1 = 1$ , whereas a value of  $K_{f_1} > 1.8$  corresponds to a PDF that has a central peak, in this case at  $\langle f_1 \rangle = 0.5$  (a Gaussian distribution of volume fraction fluctuations has a value  $K_{f_1} = 3$ ). The skewness (normalized third-order moment) of the density fluctuations was measured to be approximately zero on the centerplane, consistent with the expected symmetry of  $P(f_1)$  in this small Atwood experiment, and is not further discussed.

Figure 3 shows both the early and intermediate time-evolution of  $P(f_1)$ . At early-times ( $\tau = 0.016$  and  $\tau = 0.06$ ) the volume fraction distributions are peaked at  $f_1 = 1/2$ , indicating that most of the fluid at the centerline is mixed. However, as the initial bubbles and spikes grow ( $\tau = 0.204$  and  $\tau = 0.473$ ), a large portion of the centerplane becomes occupied by pockets of pure hot and cold water engulfed by the mixing layer, causing the distribution to become strongly bimodal. This trend is reversed at later times ( $\tau > 0.473$ ), as a central peak reemerges in the distribution of  $P(f_1)$  as  $\tau$  and the Reynolds number increase. Similar volume fraction distributions were reported by Ramaprabhu and Andrews (2004a) using lower resolution thermocouples; however, a greater degree of bimodality is reported here. The present measurement refines the measurements reported by Ramaprabhu & Andrews (2004a), as smaller thermocouples were used to better resolve the sharp density gradients present during the early stages of mixing (Mueschke & Andrews 2005).

The time-evolution of  $K_{f_1}$ , shown in Fig. 4, quantifies the modality observed in Fig. 3. The initial, single-mode distribution of  $P(f_1)$  evolves to a bimodal distribution, and the values of  $K_{f_1}(\tau)$  decrease below 1.8 correspondingly. This indicates a strong segregation of the two fluids at early and intermediate times ( $0.204 < \tau < 0.473$ ). As nonlinear interactions become increasingly dominant, the range of scales continues to increase, as do the associated interfacial areas between pockets of hot and cold fluid. Thus, as the rate of molecular diffusion increases,

so does the value of  $K_{f_1}$ .

#### 4.1.4. The degree of molecular mixing

Measured density data was also used to determine an integral measure of the degree of molecular mixing  $\theta(\tau)$  at a given downstream location. The measure of molecular mixing used here was first introduced by Dankwerts (1952) as the degree of fluid segregation. The definition of  $\theta$  requires two quantities,  $B_0$  and  $B_2$ :

$$B_0 \equiv \sigma_{f_1}^2 = \frac{\langle \rho'^2 \rangle}{(\Delta \rho)^2} \quad (8)$$

is the dimensionless variance of density fluctuations corresponding to two *miscible* fluids at a given downstream location, and

$$B_2 = \langle f_1 \rangle \langle f_2 \rangle = \langle f_1 \rangle (1 - \langle f_1 \rangle) \quad (9)$$

is the dimensionless variance of density fluctuations corresponding to two *immiscible* fluids (i.e. a pure two-fluid mixture) at a given downstream location, and is readily obtained from Eq. (8). The molecular mixing fraction at a given downstream location is then defined as

$$\theta(\tau) = 1 - \frac{B_0(\tau)}{B_2(\tau)}, \quad (10)$$

such that  $\theta = 0$  when the two fluids are completely segregated, and  $\theta = 1$  when they are completely molecularly mixed, i.e., the density is uniform. The time-evolution of the centerplane values of  $B_0$ ,  $B_2$ , and  $\theta$  are shown in Fig. 5. A dotted line is shown at a value of 0.25, which corresponds to the reported values of  $B_2$ , indicating that all measurements were taken on the centerplane.

Figure 5 reveals two stages of evolution of the molecular mixing fraction  $\theta$ . At early times ( $\tau < 0.4$ ),  $\theta$  decreases rapidly, which occurs during the early-time growth of the initial perturbations in the linear and weakly-nonlinear regimes. The second stage is characterized by an increase in  $\theta$  ( $\tau > 0.4$ ). The observed evolution of  $\theta$  suggests the following dynamical interpretation. A decrease in  $\theta$  during the first stage is attributed to the initial growth of Rayleigh-Taylor unstable perturbations, leading to a straining of the initial density interface shed from the splitter plate. At the centerplane, the two fluids are ‘stirred’ with little molecular mixing. A subsequent increase of  $\theta$  during the second stage is due to the flow complexity associated with the development of strong nonlinearities.



Secondary Kelvin-Helmholtz instabilities develop between rising bubbles and falling spikes, rapidly increasing the interfacial area between the fluids and the associated molecular diffusion. This transition is observed in the water channel experiments at  $\tau \approx 0.4$ , at which time  $\theta$  attains its minimum value. Ristorcelli and Clark (2004) noted similar dynamics in a direct numerical simulation of a small Atwood number, miscible Rayleigh-Taylor instability-driven mixing layer.

In the present experiment, the degree of molecular mixing at the centerplane of the mixing layer varies significantly over the times measured,  $0.016 \leq \tau \leq 1.36$ . The time-evolution of the volume fraction PDF, volume fraction variance and kurtosis, and molecular mixing fraction is shown in Figs. 3–5, which indicate the same early-time imbalance between the rates of fluid engulfment and molecular mixing. The term *engulfment* is used here in analogy with the term *entrainment*, typically used in shear layers in which the physical mechanism by which fluid enters the mixing layer is different from that in a Rayleigh-Taylor instability-driven mixing layer. Upon comparison of Figs. 3–5 at  $\tau \approx 0.4$ , an early-time transition point in the development of the mixing layer is observed when the rates of fluid engulfment and molecular mixing are comparable. Prior to the onset of strong nonlinearity, the growth of the initial buoyant structures engulfs *unmixed* fluid into the mixing layer before developing substantial surface area between the two fluids, thereby limiting the amount of molecular mixing. Beyond this transition point, the rate of molecular mixing due to turbulent fluctuations is greater throughout the mixing layer and, as a result, both the rate of molecular mixing and the amount of mixed fluid at the centerline increase.

The molecular mixing between two fluids in a miscible Rayleigh-Taylor mixing layer is difficult to measure due to the large number of samples required for the statistical convergence of  $\langle f_1 \rangle$  and  $\sigma_{f_1}^2$ , with the measurement points taken with sufficient spatial resolution to resolve all density gradients (Mueschke & Andrews 2005). Other researchers have typically reported values of  $\theta(z)$  across the mixing layer or  $\Theta(\tau)$  (a global measure of molecular mixing) for late times (Youngs 1991), rather than the evolution of  $\theta(z=0, \tau)$ , as reported here. Ramaprabhu and Andrews (2004a) also measured  $\theta(z=0, \tau)$  in the same water channel used in the present investigation. In the present work, a minimum value of  $\theta \approx 0.4$  was measured and occurs at the same time  $\tau \approx 0.4$  as in Ramaprabhu and Andrews (2004a), but is lower than their reported value  $\theta = 0.68$ . The difference between the measured values of  $\theta$  reported here and by Ramaprabhu and Andrews (2004a) is attributed to the difference in the size of the thermocouple probes and the noise elimination techniques used in the present work (Mueschke 2004;

Mueschke & Andrews 2005). Ristorcelli and Clark (2004) report a similar two-stage behavior of  $\theta(z = 0, \tau)$ ; however, the exact time of transition and the minimum value of  $\theta$  differ. Perhaps the difference between the present early-time measured results and the simulation results of Ristorcelli and Clark is due to the fact that the initial velocity field was zero in their numerical simulations.

#### 4.1.5. Evolution of the density variance spectrum

Consider the time-evolution of the density variance spectrum. The amplitude of the density fluctuations is given by the one-dimensional Fourier transform of the density trace

$$\begin{aligned}\hat{\rho}(k, \tau) &= \Phi[\rho(x, \tau)] \\ &= \frac{2}{L} \int_0^L \rho(x, \tau) e^{-ikx} dx,\end{aligned}\tag{11}$$

where  $\Phi$  denotes the Fourier transform,  $k \equiv 2\pi/\lambda$  is the wavenumber corresponding to wavelength  $\lambda$ , and  $L$  is the distance over which  $\rho(x)$  was measured [see Eq. (5)]. The change from temporal variation to spatial variation utilizes Taylor's hypothesis to relate  $\rho(t)$  and  $\rho(x)$  (Pope 2000). As the probe volume records pointwise measurements, the dependence of the density field upon the other spatial and temporal dimensions is suppressed for brevity. The complex-valued fluctuation amplitude and phase is given by Eq. (11), from which the one-dimensional energy spectrum is

$$E_\rho(k, \tau) = \frac{\hat{\rho}(k, \tau)^* \hat{\rho}(k, \tau)}{4 \Delta k},\tag{12}$$

where  $\hat{\rho}^*$  is the complex conjugate of  $\hat{\rho}$  and  $\Delta k = 2\pi/L$  is the wavenumber bin width. Normalization of Eq. (12) by the wavenumber bin width  $\Delta k$  results in the relationship

$$\frac{\langle \rho'^2 \rangle(\tau)}{2} = \int_0^\infty E_\rho(k, \tau) dk\tag{13}$$

in the continuum wavenumber limit.

In general, density variance spectra calculated from pointwise measurements exhibit noisy profiles due to several factors, including the finite bit-depth of the data acquisition system, finite recording time of data points, and random errors due to electronic noise. The fluctuations in  $E_\rho(k, \tau)$  render it difficult to accurately estimate the spectral slopes in various power-law regimes with any certainty. In order to elucidate possible scaling laws of the

density variance spectra, the original spectra must be smoothed. Ramaprabhu and Andrews (2004a) used Savitsky-Golay filtering techniques, which fits an  $n$ th-order polynomial to a moving window ( $2n+1$  points wide) to perform smoothing. However, significant filtering is required to smooth the intermediate-to-large wavenumber regimes of the variance spectra. The present study further improves upon this technique by implementing a smoothing procedure that conserves energy in local wavenumber regions by binning variance values to wavenumber bins,  $\Delta k$ , which increase in size *logarithmically*. This method is conservative by construction and significantly smooths the intermediate and large wavenumber regimes. As in standard discrete sampling theory, the density variance spectrum  $E_\rho(k, \tau)$  is originally sorted in wavenumber bins of constant size  $\Delta k = 2\pi/L$ . To smooth the spectra, the density variance per unit wavenumber obtained from Eq. (12) was placed into wavenumber bins logarithmically increasing in size and normalized by the local wavenumber bin width: this results in a procedure that *averages the density variance over a wavenumber bin width that increases in size at the same rate as the number of modes resolved at higher wavenumbers*. This procedure conserves the energy content of the spectrum, which was confirmed by comparing the integrals of the original spectra with those of the smoothed spectra. Figure 6 illustrates the results of the smoothing procedure by plotting the unsmoothed and smoothed spectra.

Another characteristic of experimentally measured variance spectra is the horizontal “tail” at large wavenumbers, indicating the level at which the system noise is greater than the measured fluctuations. It is possible to improve the dynamic range of  $E_\rho(k, \tau)$  measured by subtracting the system noise from the measured density variance spectrum using a Wiener filtering technique (Press *et al.* 2002). This procedure requires either an estimate or a measurement of the system noise to subtract from the measured density variance spectrum. In the present work, the background noise was measured by filling the channel with water and allowing thermal equilibrium to be attained. A thermocouple probe was placed in the water channel and a two-minute sample of the background noise was measured at 50 kHz. Fluctuations in the temperature trace, induced by EMF and RFI noise, were converted to density using Eq. (3). The variance spectrum of the background noise was calculated and subtracted from the measured density variance spectrum. This procedure provided an additional decade of measurable variance values at the largest wavenumbers. The subtraction of the background noise also eliminated a large portion of spurious noise from the initial density variance spectrum at  $\tau = 0.016$ , which will be discussed in detail next.

The early-time density variance spectra ( $\tau = 0.016$ ) are shown in Fig. 7, and exhibit broad-band

perturbations at the onset of the instability. However, the density variance spectrum at  $\tau = 0.06$  contains considerably more energy in the non-dimensional wavenumber range  $kH < 100$ ; it is hypothesized that the initial perturbations in the streamwise direction are driven by vertical velocity fluctuations. The relationship between the initial density variance spectrum and the vertical velocity variance spectrum near the edge of the splitter plate will be further discussed in § 4.1.6. While the early-time ( $\tau = 0.016$ ) spectra exhibit broad-banded energy content, the majority of the energy is contained near the peak value of  $kH \approx 90$ . The peak variance value is two orders of magnitude greater than the longest wavelength content of the spectrum. Relating the energy content to the amplitude of the perturbation,  $\|\hat{\rho}(k, \tau)\| \sim \sqrt{\langle \rho'^2 \rangle(k, \tau)}$ , yields a ratio of peak perturbation amplitude to long-wavelength perturbation amplitude of  $\hat{\rho}_{peak} / \hat{\rho}_{kH < 10} \approx 10$ . Thus, while the experiment contains longer wavelengths in the initial density spectrum, the amplitudes of these long-wavelength perturbations are much smaller than the intermediate wavelength perturbations, and are believed to contribute insignificantly to the early transitional dynamics of the mixing layer. However, any implementation of the initial conditions in a numerical simulation should retain this low wavenumber content, as longer wavelength perturbations have been shown to be important in the late-time dynamics of a Rayleigh-Taylor unstable mixing layer (Linden, Redondo & Youngs 1994; Dimonte 2004; Dimonte *et al.* 2005).

As the mixing layer develops, a steep decay in the energy spectrum is noted at larger non-dimensional wavenumbers ( $kH > 100$ ) as small-scale fluctuations are damped by diffusion, as shown in Fig. 8. However, definitive power-law scalings are difficult to determine due to the short interval over which the steep decay occurs (less than one decade). At later times ( $\tau = 0.865$  and  $\tau = 1.36$ ), a small range of scales exhibit a spectral slope of approximately  $k^{-5/3}$ , shown in Figs. 9 and 10. Compensated density variance spectra are shown in Figs. 9 and 10 as well, where the apparent inertial subrange occupies approximately one decade of wavenumbers. This slight deviation may be due to the limited Reynolds numbers attained in the experiment: Ramaprabhu and Andrews (2004a) also estimated the integral-scale Reynolds number at  $\tau = 1.21$  to be  $Re \approx 1000\text{--}1450$ , depending upon the choice of lengthscale  $L$  and velocity-scale  $U$ . Wilson and Andrews (2002) and Ramaprabhu and Andrews (2004a) reported a late-time  $k^{-5/3}$  scaling. They also showed that at  $\tau = 2.08$ , an inertial subrange for  $E_\rho(k, \tau)$  exists over approximately one decade of wavenumbers, in agreement with the current results.

## 4.2. PIV diagnostics and measurements of streamwise velocity perturbations

### 4.2.1. Description of the PIV system

Velocity perturbations in the streamwise direction were measured using particle-image velocimetry (PIV) (Adrian 1991, 2005). The PIV system consisted of two 120 mJ Nd-YAG lasers (532 nm), each with a firing rate of 15 Hz and a pulse width of 5 ns. The lasers were triggered in an alternating fashion, resulting in an effective 30 Hz sampling rate. Each 500-gallon water tank was seeded with 3.5 g of neutral-buoyancy silver spheres having a mean particle diameter of 10  $\mu\text{m}$ . A series of cylindrical lenses created a sheet of laser light in the  $xz$ -plane of the water channel, as seen in Figs. 1 and 11. The laser sheet was positioned so that the  $u$  and  $w$  (streamwise and vertical) components of the velocity field were measured in a plane just off the splitter plate. The measurements of  $u$  and  $w$  were then decomposed into their mean ( $\langle u \rangle$  and  $\langle w \rangle$ ) and fluctuating ( $u'$  and  $w'$ ) components.

Images were captured using a Kodak *Megaplot*<sup>TM</sup> digital imaging system. The image capturing system and laser triggering system were synchronized using a pulse generator (Kraft 2004). A series of 1200 images with a resolution of  $640 \times 480$  pixels was recorded using *LabVIEW*<sup>TM</sup>. The spatial resolutions of the PIV measurements are given in Table 3. Instantaneous velocity fields were determined by calculating the two-dimensional cross-correlation of two successive images using *MATPIV* (Grue *et al.* 2000; Sveen 2004). Particle displacement vectors were calculated from the cross-correlation of an interrogation window within two successive images:

$$R(x, y) = \sum_{i=-M/2}^{M/2} \sum_{j=-N/2}^{N/2} I_1(i, j) I_2(i + x, j + y), \quad (14)$$

where  $I_1$  and  $I_2$  are the two-dimensional, 8-bit scalar intensity fields recorded by the image capturing system. The particle displacement vector is defined as the distance between the center of the interrogation window and the peak of the cross-correlation function in two-dimensional space. Displacement vectors outside two standard deviations from their neighbors were discarded and replaced by interpolated values. The *MATPIV* post-processing algorithm employed a multi-pass technique, in which the initial pass operated on  $64 \times 64$  pixel interrogation windows. The second pass used displacement vectors from the first pass as initial estimates for  $32 \times 32$  pixel interrogation windows. In both the first and second pass, the interrogation windows overlapped by 50%, resulting in a final field of  $39 \times 29$  velocity vectors. To examine the velocity fluctuations at a given point in space, the  $u$  and  $w$  velocity components at a given  $(x, y)$  location were taken from each of the 1199 velocity fields. The uncertainty of the

velocity measurements was determined by Ramaprabhu (2003) to be  $\pm 0.05$  cm/s using standard methods described by Adrian (1997). The variance of the second moments  $\langle u'^2 \rangle$  and  $\langle w'^2 \rangle$  were estimated such that

$$S_{\langle \phi'^2 \rangle} \cong \frac{\frac{1}{N_{smp}} \sqrt{\langle \phi'^4 \rangle - \langle \phi'^2 \rangle^2}}{\langle \phi'^2 \rangle}, \quad (15)$$

where  $N_{smp} = 1199$  for PIV measurements (Benedict & Gould 1996). The estimated uncertainty was calculated using a 95% confidence interval, where the uncertainty is  $\pm 1.96 S_{\langle \phi'^2 \rangle}^{1/2}$ . The relative uncertainty in the horizontal and vertical velocity variances are  $\langle u'^2 \rangle \pm 4.5\%$  and  $\langle w'^2 \rangle \pm 3.0\%$  at  $\tau \approx 0.9$ . This represents a conservative error estimate, as these estimates were calculated at the furthest downstream location measured, i.e., the fewest large-scale structure were observed during the 40 second capture time interval.

#### 4.2.2. Measurement of the initial velocity perturbations at the interface

To quantify the initial velocity perturbations at the two-fluid (hot and cold water) interface, PIV measurements were performed in the wake immediately following the trailing edge of the splitter plate and end-screen (0.4–4.0 cm), as shown in Fig. 11. Velocity measurements were taken with no temperature difference between the two streams, so that the momentum disturbance generated by the experimental apparatus could be isolated from the Rayleigh-Taylor unstable configuration. The vertical velocity fluctuations measured in the wake of the splitter plate result from the separating boundary layers above and below the splitter plate. The wake Reynolds number behind the splitter plate, based on the mean velocity and splitter plate thickness, is approximately  $Re \approx 180$ , varying slightly with the mean velocity in each experiment. Flows with comparable Reynolds numbers in cylinder wakes yield unsteady, laminar von Kármán vortex sheets (Williamson 1996).

A contour plot of the vertical fluctuating velocity variance  $\langle w'^2 \rangle$  in the region following the splitter plate is shown in Fig. 12, where a small wake behind the splitter plate is visible in the peak values of  $\langle w'^2 \rangle$  (white in the figure). Figure 13 shows the evolution of  $\langle w'^2 \rangle$  at the centerline of the wake. Equations (11) and (12) are used in a similar manner to calculate  $\hat{w}(k, \tau)$  and  $E_w(k, \tau)$ . The vertical velocity variance spectrum at  $x = 1.0$  cm downstream is shown in Figure 14, and can be qualitatively related to the early-time density variance spectra shown in Fig. 7. The density spectrum at  $\tau = 0.016$  peaks at approximately  $kH \approx 90$ , or at  $k \approx 2.8 \text{ cm}^{-1}$  ( $\lambda = 2.2 \text{ cm}$ ); this

peak corresponds to the peak of the velocity spectrum at  $k \approx 3 \text{ cm}^{-1}$  ( $\lambda = 2.1 \text{ cm}$ ). The velocity spectrum contains a second local maximum at approximately  $k \approx 0.4 \text{ cm}^{-1}$  ( $15.7 \text{ cm}$ ), corresponding to a second local maximum in the density variance spectrum, seen in Fig. 7 at  $kH \approx 12$  for  $\tau = 0.016$ . This second peak in the density spectrum is less pronounced than the first peak, which is likely due to the order of magnitude decrease in energy from the first peak to the second peak in the velocity spectrum. This correlation between peaks of the vertical velocity and density variance spectra implies that the wake shedding behind the splitter plate, and hence the initial velocity fluctuations, are the dominant influence on the early-time development of the mixing layer.

In addition to comparing the peaks of the velocity and density variance spectra, it is possible to examine the rate at which energy ( $\langle w'^2 \rangle / 2$  and  $\langle \rho'^2 \rangle / 2$ ) is accumulated across a spectrum of modes in order to study the early-time evolution of the mixing layer. By examining the early-time evolution of  $E_\rho(k)$  (see Fig. 7) it is observed that a large percentage of the change in  $E_\rho(k, \tau)$  from  $\tau = 0.016$  to  $\tau = 0.06$  occurs in the smallest wavenumbers ( $kH < 50$ ). From linear stability analysis of a Rayleigh-Taylor unstable interface including viscous effects, the most unstable wavelength is

$$\lambda_m \approx 4\pi(\nu^2 A g)^{1/3} \quad (16)$$

(Chandrasekhar 1961). Taking the kinematic viscosity of the mixture  $\nu = (\mu_1 + \mu_2)/(\rho_1 + \rho_2)$  and  $A = 7.5 \times 10^{-4}$ , the most unstable wavelength is  $\lambda_m = 0.53 \text{ cm}$ , corresponding to  $kH \approx 384 \text{ cm}^{-1}$ . Linear stability analysis indicates that, in the absence of external forces and velocity fields, the high wavenumber regime of the density variance spectrum ( $kH \approx 384$ ) should accumulate energy at the greatest rate. Exponential growth of the small and intermediate wavelengths should be small; however, a greater change in the density variance spectrum is observed in the smaller wavenumber modes ( $1 < kH < 100$ ), which are not expected to grow as rapidly as the high wavenumber regime ( $kH > 100$ ). The majority of growth in these modes is attributed to velocity perturbation-driven growth of the mixing layer.

While vertical velocity fluctuations are hypothesized to be the dominant mechanism contributing to the initial development of the Rayleigh-Taylor mixing layer in the water channel experiment, the current set of measurements allow second-order effects at  $\tau = 0$  to be measured as well, such as the value of the velocity deficit in the wake trailing the splitter plate. Ramaprabhu (2003) reported a velocity deficit of approximately 10% of the mean

advection velocity at a distance  $x = 1.0$  cm from the splitter plate. This deficit was found to be negligible at  $x = 2.0$  cm, as buoyancy effects began to dominate the mixing layer dynamics. A contour plot of  $\langle u \rangle$  is shown in Fig. 15, and the decrease in  $U_m$  (the velocity deficit) at the edge of the splitter plate is evident. The current measurements exhibit a 5% difference between the mean advection velocity ( $U_m = 5.15$  cm/s) and the minimum velocity within the wake ( $u_{min} = 4.9$  cm/s) at  $x = 1.0$  cm downstream. This reduction in the velocity deficit behind the splitter plate is attributed to the existence of smaller boundary layers at the knife-edge of the splitter plate, which are a result of modifications to the upstream screen meshes (Mueschke 2004).

#### 4.2.3. Evolution of velocity variances, probability distribution functions, and spectra

The evolution of the horizontal and vertical velocity variances,  $\langle u'^2 \rangle$  and  $\langle w'^2 \rangle$  respectively, at the centerplane of the mixing layer was quantified by taking measurements at multiple downstream locations. The evolution of  $\langle u'^2 \rangle$  and  $\langle w'^2 \rangle$  is shown in Fig. 16. Small variations in each experimental run account for the range of variance values reported. Both  $\langle u'^2 \rangle$  and  $\langle w'^2 \rangle$  are originally very small in magnitude, although finite. During the initial development of the mixing layer, vertical velocity fluctuations grow more rapidly than horizontal fluctuations as a consequence of the continuous forcing in the gravitational direction and vertical direction, with little energy transferred from the vertical to horizontal directions by secondary instabilities and turbulent fluctuations. At  $\tau = 0.2$ , the ratio of vertical to horizontal velocity variances is approximately  $\langle w'^2 \rangle / \langle u'^2 \rangle \approx 5.6$ . This ratio remains relatively stationary, where at  $\tau = 0.5$ ,  $\langle w'^2 \rangle / \langle u'^2 \rangle \approx 5.8$ . However, as turbulent motions and more three-dimensional structure develop, the ratio decreases slightly to  $\langle w'^2 \rangle / \langle u'^2 \rangle \approx 4.4$  as more energy is contained in the horizontal velocity fluctuations. This ratio can also be seen in the probability density functions of  $u'$  and  $w'$ , shown in Fig. 17. The second moments  $\langle u'^2 \rangle$  and  $\langle w'^2 \rangle$  are a measure of the spread of  $P(u')$  and  $P(w')$ . At each time shown in Fig. 17, the vertical velocity fluctuations exhibit a much greater range of values.

In addition to the evolution of  $\langle u'^2 \rangle$  and  $\langle w'^2 \rangle$ , the spectral evolution of  $E_u(k)$  and  $E_w(k)$  at the centerplane are examined at various times, and are shown in Figs. 18 and 19. At the earliest times ( $\tau = 0.017$  and  $\tau = 0.307$ ), the peak energy values in the vertical velocity fluctuations at  $kH \approx 10$  and  $kH \approx 100$  can be clearly seen. These peaks correspond to the peak values measured in the non-buoyant arrangement, shown in Fig. 14. At later times ( $\tau = 0.582$  and  $\tau = 0.920$ ), these peaks are no longer distinct features of the spectrum. As the initial dominant



modes saturate, nonlinear dynamics result in significant spectral energy transfer to modes above and below the wavenumber peaks at  $kH \approx 10$  and  $kH \approx 100$ . As a cascade of energy to smaller scales develop, an approximate  $k^{-3}$  dissipative subrange scaling develops at  $\tau = 0.582$  and  $\tau = 0.920$  (Fig. 19). This scaling has been noted by previous researchers examining Rayleigh-Taylor unstable flows (Wilson 2002; Ramaprabhu & Andrews 2004a). While no formal phenomenology or theory has been developed to explain such a scaling, similar results have been reported by researchers investigating turbulent buoyant plumes (Papanicolaou & List 1987; Dai *et al.* 1994; Fisher & Ball 1999). Also, in this higher wavenumber regime, the vertical velocity fluctuations can be seen contain almost one order of magnitude more energy than the horizontal fluctuations. This anisotropy is sustained even to the smallest scales measured.

### 4.3. PLIF diagnostics and measurements of the spanwise interfacial perturbation

#### 4.3.1. Description of the PLIF system

Planar laser-induced fluorescence (PLIF) was used to measure the interfacial perturbations in the spanwise ( $y$ ) direction. PLIF detects the presence of a scalar by seeding one fluid stream with a dye that fluoresces when excited by a specific wavelength of laser light (Jacobs 1992; Lee *et al.* 1992). To perform the PLIF measurements, the current optical arrangement of the PIV system was modified so that the laser sheet was perpendicular to the mean channel flow. A schematic of the camera and laser sheet arrangement is shown in Fig. 20. Rhodamine 6G dye (2.5 g) was added to the 500-gallon tank containing the top (cold) stream such that it would fluoresce in the presence of 532 nm laser light. The laser sheet was placed a distance  $x = 0.5$  cm from the trailing edge of the splitter plate so that only the top stream was illuminated, thereby allowing the determination of the two-fluid interfacial perturbation. The digital imaging system used in the thermocouple and PIV experiments was modified to record images of  $1000 \times 480$  pixels over a domain size of approximately  $10 \text{ cm} \times 5 \text{ cm}$ . The imaging system was synchronized with the laser system in the same manner as in the PIV configuration (Kraft 2004).

One potential concern with the use of PLIF in the water channel is that the diffusivity of heat and the diffusivity of the fluorescing dye marker are very different. As a temperature difference between the two streams is used to induce the density difference, the two-fluid mixture is miscible with a Prandtl number  $Pr = \nu / D \approx 7$ , where  $\nu$  and  $D$  are the kinematic viscosity and thermal diffusivity of water, respectively. However, Rhodamine 6G dye in

the top stream diffuses into the bottom stream at a much slower rate than the diffusion of heat, where the Lewis number is  $Le \equiv Pr/Sc \sim 10^3$ . This raises the question of whether the dye is an accurate marker for the two-fluid interface. This error was minimized in the current investigation by taking measurements in the limit of  $\tau \rightarrow 0$ , i.e. near the splitter plate, such that the difference between the amounts of diffusion is negligible. As there is insufficient time for significant thermal diffusion to occur, the dye can be regarded as an accurate marker for the cold water stream. Other than the negligible difference in the diffusion at early times, the location of the two-fluid interface is the only desired information from the measurement, rather than data pertaining to the internal flow structure.

#### 4.3.2. Measurement of spanwise interfacial perturbations and image dewarping

Spanwise interfacial measurements were performed as follows. First, the laser head and all associated optics were configured such that a vertical laser sheet was formed in a plane  $x = 0.5$  cm downstream from the splitter plate. The camera was located approximately 50 cm from the midpoint of the trailing edge of the splitter plate, and the focal axis was located on the same horizontal plane as the splitter plate at an angle approximately  $35^\circ$  with respect to the axis normal to the laser sheet. The laser sheet was focused so that its thickness was less than 1 mm near the centerplane of the mixing layer. Using a syringe, a solution of Rhodamine 6G dye and water was injected into the channel so that the imaging system could be focused. Once the camera was focused, the water channel pumps were activated, the mean advection velocities of each stream were adjusted to eliminate any shear, and then a series of images of the fluorescing dye were captured. For reasons discussed earlier, the water channel was operated with no temperature difference between the two streams. Measurements were also performed at  $A \approx 5.0 \times 10^{-4}$ , with no difference found between the measurements performed at  $A = 0$ . Thus, the measured perturbations represent the interfacial perturbation imposed by the splitter plate and end-screen on the two-fluid interface in the spanwise direction. Once images of the two-fluid interface had been captured, the water channel was drained and a calibration card was placed at the same location as the laser sheet. The calibration card consisted of a grid of horizontal and vertical lines located at 1.27 cm intervals, and was used to eliminate any parallax and perspective errors introduced by positioning the camera at an oblique angle to the laser sheet. The calibration card was mounted between two sheets of clear 0.64 cm thick Plexiglas to ensure that the card remained flat during the course of an experiment. Once the calibration card was in place, an image of the grid was recorded with the same camera settings and location

used to capture the PLIF images. Images of the grid were used as a fiducial to calibrate the dewarping procedure described next.

Special consideration was given to the dewarping of the spanwise images. Other researchers have used off-axis imaging and dewarping algorithms in stereoscopic PIV (Arroyo & Greated 1991; Willert 1997) and in other applications (Kent & Eaton 1982). However, the present experiments differ from previous implementations of off-axis imaging. The procedure used in the present investigation is the same robust, second-order dewarping method discussed by Pratt (1991) and van Oord (1997). The functional relationship between the warped coordinates  $(X_w, Y_w)$  and the dewarped coordinates  $(X_d, Y_d)$  is given by a second-order polynomial

$$\begin{aligned} X_d(X_w, Y_w) &= a_0 + a_1 X_w + a_2 Y_w + a_3 X_w Y_w + a_4 X_w^2 + a_5 Y_w^2, \\ Y_d(X_w, Y_w) &= b_0 + b_1 X_w + b_2 Y_w + b_3 X_w Y_w + b_4 X_w^2 + b_5 Y_w^2, \end{aligned} \quad (17)$$

where the  $a_i$  and  $b_i$ ,  $i = 1-5$ , are calibrated coefficients. The unknown coefficients were determined from a least-squares fit relating fifteen control points from the warped image of the calibration grid to their true physical location. Figure 21 shows the raw warped image of the calibration grid and a corrected image. A corrected PLIF image of the spanwise interfacial perturbation is shown in Fig. 22. Once a PLIF image has been corrected for perspective errors, the two-fluid interface was extracted by analyzing the intensity values at each pixel location of the image. A Canny-type edge filter (Canny 1986) was used to determine the interface between the fluorescing and non-fluorescing fluids. The Canny method identifies edges in the image at local maxima of the gradient of the intensity field, given a threshold value to eliminate spurious boundaries.

#### 4.3.3. The interfacial perturbation spectrum

Having measured the interfacial perturbation in the spanwise direction  $\zeta(y)$ , a corresponding variance spectrum  $E_\zeta(k, \tau)$  was computed. Figure 23 shows the interfacial perturbation spectrum for one captured image, with other images yielding similar spectra. The spectrum is broad-banded, with most of the energy content in the intermediate wavelengths  $0.16 < \lambda < 5.0$  cm, well within the water channel width of 20 cm. The maximum 5 cm wavelength is attributed to the maximum width of the laser sheet achievable at the two-fluid interface. A  $k^{-2}$  scaling is evident in the wavenumber range of approximately  $10 < k < 300$ . This measured interfacial spectrum is similar to the spectrum of the surface roughness of glass ICF capsules which have measured interfacial perturbations that scale

as  $k^{-2}$  in the lowest decade of modes (Milovich *et al.* 2004; Dimonte 2004).

Another result observed from the spanwise PLIF measurements was that the interfacial perturbation contained no observable temporal oscillations in the spanwise direction, suggesting that perturbations created by the splitter plate and end screen do not include a velocity component in the spanwise direction. This observation eliminates the need to perform velocity measurements in the  $yz$ -plane. In addition, a model of the initial conditions of the experiment can be further simplified to include only velocity perturbations in the  $xz$ -plane.

The present measurements describe an initially-anisotropic state in which the interfacial perturbations in the streamwise ( $x$ ) and spanwise ( $y$ ) directions are independent of one another and the only velocity perturbations large enough to be measured exist in the streamwise direction. Anisotropy of the initial conditions is expected when the initial perturbations are imposed by the experimental design. Examples of experimentally-imposed initial conditions include: oscillation of separating boundary layers from the termination of the splitter plate in this experiment and in plate-withdrawal experiments (Linden & Redondo 1991; Linden, Redondo & Youngs 1994; Dalziel, Linden & Youngs 1999); oscillation of accelerating tank experiments to produce a nominally two-dimensional perturbation (Emmons, Chang & Watson 1960; Ratafia 1973; Cole 1973; Popil & Curzon 1979), and; planar or spherical laser-driven experiments that include surface perturbations at material interfaces (Kilkenny *et al.* 1994; Lindl 1998; Oron *et al.* 1999). It is difficult to quantify the initial perturbations in experiments that impose perturbations in two dimensions; however, several such experiments have yielded measurements for the single-mode instability evolution (Jacobs 1988; Wilkinson 2004). Additional modeling issues involving the specification of initial conditions are briefly discussed below.

## **5. Implications of the experimental results for the initialization of turbulent transport models and numerical simulations**

An outstanding issue in turbulent transport modeling using the Reynolds-averaged Navier-Stokes (RANS) equations and other modeling approaches is the specification of the initial conditions satisfied by the turbulent fields. Moreover, the predictions of RANS models are inherently sensitive to the initial conditions chosen. The current initialization of RANS models is typically *ad hoc* and is often an iterative procedure involving the adjustment of

model parameters and initial conditions until satisfactory predictions of mean flow quantities and low-order statistics are obtained. The initialization of RANS models to describe turbulent mixing induced by hydrodynamic instabilities, such as the Rayleigh-Taylor instability, presents several particular issues. Often turbulent transport models applied to Rayleigh-Taylor mixing are initialized using a phenomenological buoyancy-drag model to evolve the velocity fluctuations until the width of the mixing layer becomes approximately equal to  $2\Delta x$ , where  $\Delta x$  is the grid spacing, at which time the fluctuations are used to provide an initial value of the turbulent kinetic energy, as in the *K-l* model of Youngs (1989, 1994). Similar issues are also shared by large-eddy simulation (LES) of hydrodynamic instability-driven turbulent mixing in which the large scales are generated from small scales. In particular, the scale of the initial perturbations may be smaller than the grid size in either a transport model or in an LES, which raises the issue of how energy production at these unresolved small scales feeds into the turbulent transport quantities being evolved or into the explicit subgrid-scale model in an LES. However, LES of Rayleigh-Taylor instability-driven mixing is possible given a spatial resolution capable of resolving the initial perturbations (Cook, Cabot & Miller 2004).

In addition to complications associated with resolving the initial perturbations in a RANS model or an LES, additional issues arise from the physical nature of the perturbations. In the present work, *the spectra of velocity and density perturbations are highly anisotropic*. There are several turbulent transport and subgrid-scale modelling implications associated with identifying and investigating the anisotropic state of the initial conditions. In numerical studies investigating the effects of multi-mode initial conditions on the evolution of Rayleigh-Taylor instability-driven mixing layers, an *isotropic* spectrum of initial interfacial perturbations is typically assumed (Youngs 1981; 1994; Cook & Dimotakis 2001; Cook, Cabot and Miller 2004; Dimonte *et al.* 2004; Ristorcelli & Clark 2004; Ramaprabhu & Andrews 2004b). While the specific objectives of each study vary, the use of isotropic initial conditions represents idealized initial conditions for Rayleigh-Taylor instabilities, rather than an examination of a physical experiment or an application in which the Rayleigh-Taylor instability develops. For example, the evaluation of ICF target shell designs for the National Ignition Facility (NIF) at the Lawrence Livermore National Laboratory requires accurate modeling or simulation of the hydrodynamics and mixing (Haan *et al.* 1995, 2004; Amendt *et al.* 2002; Milovich *et al.* 2004). The perturbations present on the material interfaces in ICF capsules do not generally have an isotropic spectrum. Thus, turbulent transport and mixing models that do not include the

detailed anisotropic structure of a mixing layer at early times (Youngs 1989; Steinkamp, Clark & Harlow 1999; Llor 2003) may not accurately model the unresolved hydrodynamics and mixing in imploding ICF capsules.

## 6. Summary and conclusions

The initial multi-mode interfacial and velocity conditions have been experimentally measured in both the streamwise and spanwise directions in a statistically-stationary, miscible Rayleigh-Taylor instability-driven mixing layer. This investigation both extends and refines previous work on the measurement of the initial conditions in Rayleigh-Taylor instability-driven mixing layers. The inclusion of spanwise measurements in the current characterization of the initial conditions is novel with respect to the study of Rayleigh-Taylor instability-driven flows, both in the measurement techniques used and in the results obtained. *Combined with the streamwise density and velocity measurements, the measurements presented here represent the most complete characterization of two-dimensional, multi-mode initial interfacial perturbations with velocity conditions in a Rayleigh-Taylor mixing layer to date.* Comparisons of the initial density variance and vertical velocity variance spectra indicate that the initial evolution of density scales are driven by velocity fluctuations. The measurements of the initial conditions have also shown that the initial interfacial and velocity perturbations are anisotropic in nature. This observation is important in that many models of Rayleigh-Taylor mixing layer growth do not consider either the anisotropic initial conditions or the transition from a primarily anisotropic state to a less anisotropic state in the late-time turbulent stage of the flow. Numerical simulations of a physical Rayleigh-Taylor mixing experiment must incorporate anisotropy into the initial conditions. The spectra of the initial fluctuations sufficient for the initialization of three-dimensional simulations of the water channel experiment have been presented in Figs. 7, 14, and 23.

In addition to a detailed characterization of the initial conditions of a Rayleigh-Taylor unstable fluid configuration, the time-evolution of the volume fraction probability distribution function, volume fraction variance and kurtosis, molecular mixing fraction, and density variance spectra were measured for  $0 < \tau \leq 1.36$ . These measurements indicate that an early-time transition exists in the level of molecular mixing in which, before the onset of strong nonlinearities and secondary Kelvin-Helmholtz instabilities, the interfacial area between the two fluids remains relatively small when compared to the area at later times. However, after the early-time onset of strong

nonlinearities, the degree of molecular mixing within the flow steadily increases. It was shown that this increase in  $\theta$  is associated with the decrease in  $\langle f_1'^2 \rangle$  and with the shift in the energy-containing modes to smaller wavenumbers. The experimental data obtained in the present research has clearly elucidated the complex initial conditions that are typically present in an experiment. In addition, this work has investigated the linear and nonlinear growth of the Rayleigh-Taylor instability (depending on the initial perturbation amplitudes and wavelengths), mode-coupling and growth of successively larger scales, and the transition to a well-mixed state. It is anticipated that this data, when coupled with high-resolution data from direct numerical simulations, can be used to develop criteria for the specification of initial conditions for both RANS models and for LES.

### **Acknowledgements**

The authors thank Praveen Ramaprabhu and Wayne Kraft for their insightful comments on this research. This research was sponsored by the U.S. DOE National Nuclear Security Administration under the Stewardship Science Academic Alliances program through DOE Research Grant #DE-FG03-02NA00060. This work was also performed under the auspices of the U.S. Department of Energy by the University of California, Lawrence Livermore National Laboratory under Contract No. W-7405-Eng-48.

## REFERENCES

- Adrian, R. J. 1991 Particle-imaging techniques for experimental fluid mechanics. *Ann. Rev. Fluid Mech.* **23**, 261–304.
- Adrian, R. J. 1997 Dynamic ranges of velocity and spatial resolution of particle image velocimetry. *Meas. Sci. Technol.* **8**, 1393–1398.
- Adrian, R. J. 2005 Twenty years of particle image velocimetry. *Exp. in Fluids* **39**, 159–169.
- Allred, J. C., Blount, G. H. & Miller III, J. H. 1954 Experimental Studies of Taylor Instability. Los Alamos Scientific Laboratory Report LA-1600.
- Amendt, P., Colvin, J. D., Tipton, R. E., Hinkel, D. E., Edwards, M. J., Landen, O. L., Ramshaw, J. D., Suter, L. J., Varnum, W. S. & Watt, R. G. 2002 Indirect-drive noncryogenic double-shell ignition targets for the National Ignition Facility: Design and analysis. *Phys. Plasmas* **9**, 2221–2233.
- Andrews, M. J. 1986 Turbulent mixing by Rayleigh-Taylor instability. Ph.D. thesis. Imperial College of Science and Technology, London.
- Andrews, M. J. & Spalding, D. B. 1990 A simple experiment to investigate two-dimensional mixing by Rayleigh-Taylor instability. *Phys. Fluids A* **2**, 922–927.
- Anuchina, N. N., Kucherenko, Y. A., Neuvazhaev, V. E., Ogibina, V. N., Shibarshov, L. I. & Yakovlev, V. G. 1978 Turbulent mixing at an accelerating interface between liquids of different densities. *Izv. Akad. Nauk. SSSR, Mekh. Zhidk. Gaza* **6**, 157–160.
- Arroyo, M. P. & Greated, C. A. 1991 Stereoscopic particle image velocimetry. *Meas. Sci. Technol.* **2**, 1181–1186.
- Bell, J. H. & Mehta, R. D. 1993 Effects of imposed spanwise perturbations on plane mixing-layer structure. *J. Fluid Mech.* **257**, 33–63.
- Benedict, L. H. & Gould, R. D. 1996 Towards better uncertainty estimates for turbulence statistics. *Exp. Fluids* **22**, 129–136.
- Bradshaw, P. 1966 The effect of initial conditions on the development of a free shear layer. *J. Fluid Mech.* **26**, 225–236.
- Brouillette, M. 2002 The Richtmyer-Meshkov Instability. *Ann. Rev. Fluid Mech.* **34**, 445–468.
- Browand, F. K. & Weidman, P. D. 1976 Large scales in the developing mixing layer. *J. Fluid Mech.* **76**, 127–144.



- Brown, G. L. & Roshko, A. 1974 On density effects and large structure in turbulent mixing layers. *J. Fluid Mech.* **64**, 775–816.
- Canny, J. 1986 A Computational Approach to Edge Detection. *IEEE Transactions on Pattern Analysis and Machine Intelligence* **PAMI-8**, 679–698.
- Chandrasekhar, S. 1961 *Hydrodynamic and Hydromagnetic Stability*. Dover.
- Cole, R. L. & Tankin, R. S. 1973 Experimental study of Taylor instability. *Phys. Fluids* **16**, 1810–1820.
- Cook, A. W., Cabot, W. & Miller, P. L. 2004 The mixing transition in Rayleigh-Taylor instability. *J. Fluid Mech.* **511**, 333–362.
- Cook, A. W. & Dimotakis, P. E. 2001 Transition stages of Rayleigh-Taylor instability between miscible fluids. *J. Fluid Mech.* **443**, 69–99; Corrigendum. *J. Fluid Mech.* **457**, 410–411 (2002).
- Criminale, W., Jackson, T. L. & Joslin, R. D. 2003 *Theory and Computation in Hydrodynamic Stability*, Cambridge Monographs on Mechanics. Cambridge University Press.
- Dai, Z., Tseng, L. K. & Faeth, G. M. 1994 Structure of round, fully developed, buoyant turbulent plumes. *J. Heat Transfer* **116**, 409–417.
- Dalziel, S. B., Linden, P. F. & Youngs, D. L. 1999 Self-similarity and internal structure of turbulence induced by Rayleigh-Taylor instability. *J. Fluid Mech.* **399**, 1–48.
- Dankwerts, P. V. 1952 The definition and measurement of some characteristics of mixtures. *Appl. Sci. Res.* **3**, 279–296.
- Darbyshire, A. G. & Mullin, T. 1995 Transition to turbulence in constant-mass-flux pipe flow. *J. Fluid Mech.* **289**, 83–114.
- Dimonte, G. 1999 Nonlinear evolution of the Rayleigh-Taylor and Richtmyer-Meshkov instabilities. *Phys. Plasmas* **6**, 2009–2015.
- Dimonte, G. 2004 Dependence of turbulent Rayleigh-Taylor instability on initial perturbations. *Phys. Rev. E* **69**, 1–14.
- Dimonte, G., Ramaprabhu, P., Youngs, D. L. Andrews, M. J. & Rosner, R. 2005 Recent advances in the turbulent Rayleigh-Taylor instability. *Phys. Plasmas* **12**, 1–6.
- Dimonte, G. & Schneider M. 1996 Turbulent Rayleigh-Taylor instability experiments with variable acceleration.

- Phys. Rev. E* **54**, 3740–3743.
- Dimonte, G., Youngs, D. L., Dimits, A., Weber, S., Marinak, M., Wunsch, S., Garasi, C., Robinson, A., Andrews, M. J., Ramaprabhu, P., Calder, A. C., Fryxell, B., Biello, J., Dursi, L., MacNeice, P., Olson, K., Ricker, P., Rosner, R., Timmes, H., Tufo, H., Young, Y.-N., & Zingale, M. 2004 A comparative study of the turbulent Rayleigh-Taylor (RT) instability using high-resolution 3D numerical simulations: The Alpha-Group collaboration. *Phys. Fluids* **16**, 1668–1693.
- Drazin, P. G. 2002 *Introduction to Hydrodynamic Stability*, Cambridge Texts in Applied Mathematics Vol. 32. Cambridge University Press.
- Drazin, P. G. & Reid, W. H. 2004 *Hydrodynamic Stability*, second edition. Cambridge University Press.
- Emmons, H. W., Chang, C. T. & Watson, B. C. 1960 Taylor instability of finite surface waves. *J. Fluid Mech.* **7**, 177–193.
- Faisst, H. & Eckhardt, B. 2004 Sensitive dependence on initial conditions in transition to turbulence in pipe flow. *J. Fluid Mech.* **504**, 343–352.
- Fisher, C. E. & Ball, K. S. 1999 Plume dynamics in natural convection in a horizontal cylindrical annulus. *J. Heat Transfer* **121**, 598–602.
- Grue, J., Jensen, A., Rusas, P. & Sveen, J. K. 2000 Breaking and broadening of internal waves. *J. Fluid Mech.* **413**, 181–217.
- Haan, S. W. 1989 Onset of nonlinear saturation for Rayleigh-Taylor growth in the presence of a full spectrum of modes. *Phys. Rev. A* **39**, 5812–5825.
- Haan, S. W., Amendt, P. A., Dittrich, T. R., Hammel, B. A., Hatchett, S. P., Herrmann, M. C., Hurricane, O. A., Jones, O. S., Lindl, J. D., Marinak, M. M., Munro, D., Pollaine, S. M., Salmonson, J. D., Strobel, G. L., & Suter, L. J. 2004 Design and simulation of indirect drive ignition targets for NIF. *Nucl. Fusion* **44**, S171–S176.
- Haan, S. W., Pollaine, S. M., Lindl, J. D., Suter, L. J., Berger, R. L., Powers, L. V., Alley, W. E., Amendt, P. A., Futterman, J. A., Levedahl, W. K., Rosen, M. D., Rowley, D. P., Sacks, R. A., Shestakov, A. I., Strobel, G. L., Tabak, M., Weber, S. V., Zimmerman, G. B., Krauser, W. J., Wilson, D. C., Coggeshall, S. V., Harris, D. B., Hoffman, N. M., Wilde, B. H. 1995 Design and modeling of ignition targets for the National Ignition Facility. *Phys. Plasmas* **2**, 2480–2487.

- Husain, Z. D. & Hussain, A. K. M. F. 1979 Axisymmetric mixing layer: Influence of the initial and boundary conditions. *AIAA J.* **17**, 48–55.
- Jacobs, J. W. 1992 Shock-induced mixing of a light-gas cylinder. *J. Fluid Mech.* **234**, 629–649.
- Jacobs, J. W. & Catton, I. 1988 Three-dimensional Rayleigh-Taylor instability. Part 2. Experiment. *J. Fluid Mech.* **187**, 353–371.
- Kent, J. C. & Eaton, A. R. 1982 Stereo photography of neutral density He-filled bubbles for 3-D fluid motion studies in an engine cylinder. *Appl. Opt.* **21**, 904–912.
- Kilkenny, J. D., Glendinning, S. G., Hann, S. W., Hammel, B. A., Lindl, J. D., Munro, D., Remington, B. A., Weber, S. V., Knauer, J. P., & Verdon, C. P. 1994 A review of the ablative stabilization of the Rayleigh-Taylor instability in regimes relevant to inertial confinement fusion. *Phys. Plasmas* **1**, 1379–1389.
- Koochesfahani, M. M. & Dimotakis, P. E. 1986 Mixing and chemical reactions in a turbulent liquid mixing layer. *J. Fluid Mech.* **170**, 83–112.
- Koop, G. K. 1976 Instability and turbulence in a stratified shear layer. Ph.D. thesis. University of Southern California.
- Kraft, W. N. 2004 Experimental investigation of a stratified buoyant wake. M.S. thesis. Texas A&M University.
- Kucherenko, Yu. A., Neuvazhaev, V. E. & Pylaev, A. P. 1994 Behavior of a region of gravity-induced turbulent mixing under conditions leading to separation. *Dokl. Akad. Nauk* **39**, 114–117.
- Kucherenko, Yu. A., Balabin, S. I., Cherret, R. & Haas, J.-F. 1997 Experimental investigation into inertial properties of Rayleigh-Taylor turbulence. *Las. Part. Beams* **15**, 25–31.
- Kucherenko, Yu. A., Balabin, S. I., Ardashova, R. I., Kozelkov, O. E., Dulov, A. V. & Romanov, I. A. 2003a Experimental study of the influence of the stabilizing properties of transitional layers on the turbulent mixing evolution. *Las. Part. Beams* **21**, 369–373.
- Kucherenko, Yu. A., Pylaev, A. P., Murzakov, V. D., Belomestnih, A. V., Popov, V. N. & Tyaktev, A. A. 2003b Experimental study into the Rayleigh-Taylor turbulent mixing zone heterogeneous structure. *Las. Part. Beams* **21**, 375–379.
- Kukulka, D. J. 1981 Thermodynamic and transport properties of pure and saline water. M.S. thesis, State University of New York at Buffalo.

- Lee, M. P., McMillin, B. K., Palmer, J. L. & Hanson, R. K. 1992 Planar Fluorescence imaging of a transverse jet in a supersonic cross-flow. *J. Prop. Power* **8**, 729–735.
- Linden P. F. & Redondo, J. M. 1991 Molecular mixing in Rayleigh-Taylor instability. Part I: Global mixing. *Phys. Fluids A* **3**, 1269–1277.
- Linden P. F., Redondo, J. M. & Youngs D. L. 1994 Molecular mixing in Rayleigh-Taylor instability. *J. Fluid Mech.* **265**, 97–124.
- Lindl, J. D. 1998 *Inertial Confinement Fusion: The Quest for Ignition and Energy Gain using Indirect Drive*. Springer-Verlag.
- Llor, A. 2003 Bulk turbulent transport and structure in Rayleigh-Taylor, Richtmyer-Meshkov, and variable acceleration instabilities. *Las. Part. Beams* **21**, 305–310.
- Marmottant, P. & Villermaux, E. 2004 On spray formation. *J. Fluid Mech.* **498**, 73–111.
- Meyer, T. R., Dutton, J. C. & Lucht, R. P. 2001 Experimental study of the mixing transition in a gaseous axisymmetric jet. *Phys. Fluids* **13**, 3411–3424.
- Mi, J., Nobes, D. S. & Nathan, G. J. 2001 Influence of jet exit conditions on the passive scalar field of an axisymmetric jet. *J. Fluid Mech.* **432**, 91–125.
- Milovich, J. L., Amendt, P., Marinak, M. & Robey, H. 2004 Multimode short-wavelength perturbation growth studies for the National Ignition Facility double-shell ignition target designs. *Phys. Plasmas* **11**, 1552–1568.
- Mueschke, N. J. 2004 An investigation of the influence of initial conditions on Rayleigh-Taylor mixing. M.S. Thesis, Texas A&M University.
- Mueschke, N. J. & Andrews, M. J. 2005 Investigation of scalar measurement error in diffusion and mixing processes. *Exp. Fluids* (in press).
- Oron, D., Sadot, O., Srebro, Y., Rikanati, A., Yedvab, Y., Alon, U., Erez, L., Erez, G., Ben-Dor, G., Levin, L. A., Ofer, D. & Shvarts, D. 1999 Studies in the nonlinear evolution of the Rayleigh-Taylor and Richtmyer-Meshkov instabilities and their role in inertial confinement fusion. *Las. Part. Beams* **17**, 465–475.
- Papanicolaou P. N. & List E. J. 1987 Statistical and spectral properties of tracer concentration in round buoyant jets. *Int. J. Heat Mass Transf.* **30**, 2059–2071.
- Pope, S. B. 2000 *Turbulent Flows*. Cambridge University Press.

- Popil, R. & Curzon, F. L. 1979 Production of reproducible Rayleigh-Taylor instabilities. *Rev. Sci. Instr.* **50**, 1291–1295.
- Pratt W. K. 1991 *Digital Image Processing*, second edition. Wiley.
- Press, W. H., Teukolsky, S. A., Vetterling, W. T. & Flannery, B. P. 2002 *Numerical Recipes in C: The Art of Scientific Computing*, second edition. Cambridge University Press.
- Ramaprabhu, P. 2003 On the dynamics of Rayleigh-Taylor mixing. Ph.D. dissertation. Texas A&M University.
- Ramaprabhu, P. & Andrews, M. 2003 Simultaneous measurements of velocity and density in buoyancy-driven mixing. *Exp. Fluids* **34**, 98–106.
- Ramaprabhu, P. & Andrews, M. J. 2004a Experimental investigation of Rayleigh-Taylor mixing at small Atwood numbers. *J. Fluid Mech.* **502**, 233–271.
- Ramaprabhu, P. & Andrews, M. J. 2004b On the initialization of Rayleigh-Taylor simulations. *Phys. Fluids* **16**, L59–L62.
- Ramaprabhu, P., Dimonte, G. & Andrews, M. J. 2005 A numerical study of the influence of initial perturbations on the turbulent Rayleigh-Taylor instability. *J. Fluid Mech.* **536**, 285–319.
- Ratafia, M. 1973 Experimental investigation of turbulent mixing by Rayleigh-Taylor instability. *Phys. Fluids* **16**, 1207–1210.
- Rayleigh, L. 1884 Investigation of the equilibrium of an incompressible heavy fluid of variable density. *Proc. London Math. Soc.* **14**, 170–177.
- Read, K. I. 1984 Experimental investigation of turbulent mixing by Rayleigh-Taylor instability. *Physica D* **12**, 45–58.
- Reynolds, O. 1883 An experimental investigation of the circumstances which determine whether the motion of water in parallel channels shall be direct or sinuous and of the law of resistance in parallel channels. *Philos. Trans.* **186**, 123–164.
- Ristorcelli, J. R. & Clark, T. T. 2004 Rayleigh–Taylor turbulence: self-similar analysis and direct numerical simulations. *J. Fluid Mech.* **507**, 213–253.
- Sharp, D. H. 1984 An overview of Rayleigh-Taylor instability. *Physica D* **12**, 3–18.
- Snider, D. M. & Andrews, M. J. 1994 Rayleigh-Taylor and shear driven mixing with an unstable thermal

- stratification. *Phys. Fluids A* **6**, 3324–3334.
- Steinkamp, M. J., Clark T. T. & Harlow F. H. 1999 Two-point description of two-fluid turbulent mixing - I. Model formulation. *Int. J. Multiphase Flow* **25**, 599–637.
- Stillinger, D. C., Head, M. J., Helland, K. N. & Van Atta, C. W. 1983 A closed loop gravity-driven water channel for density stratified shear flow. *J. Fluid Mech.* **131**, 73–89.
- Sveen, J. K. 2004 An introduction to MatPIV v. 1.6.1. eprint series, *Mech. and Appl. Math.* **2**, 1–27.
- Taylor, G. I. 1938 The spectrum of turbulence. *Proc. Royal Soc. London Ser. A* **164**, 476–490.
- Taylor, G. I. 1950 The instability of liquid surfaces when accelerated in a direction perpendicular to their planes. *Proc. Royal Soc. London* **201**, 192–196.
- Tennekes, H. & Lumley, J. L. 1972 *A First Course in Turbulence*. MIT Press.
- van Oord, J. 1997 The design of a stereoscopic DPIV-system. *Delft University of Technology Report* MEAH-161.
- Weygandt, J. H. & Mehta, R. D. 1995 Three-dimensional structure of straight and curved plane wakes. *J. Fluid Mech.* **282**, 279–311.
- Wilkinson, J. P. 2004 Experimental study of the three-dimensional Rayleigh Taylor instability for low Atwood numbers. M.S. thesis, University of Arizona.
- Willert, C. 1997 Stereoscopic digital particle image velocimetry for application in wind tunnel flows. *Meas. Sci. Technol.* **8**, 1465–1479.
- Williamson, C. H. K. 1996 Vortex dynamics in the cylinder wake. *Ann. Rev. Fluid Mech.* **28**, 477–539.
- Wilson, P. N. 2002 A study of buoyancy and shear driven turbulence within a closed water channel. Ph.D. dissertation. Texas A&M University.
- Wilson, P. N. & Andrews, M. J. 2002 Spectral measurements of Rayleigh-Taylor mixing at low-Atwood number. *Phys. Fluids A* **14**, 938–945.
- Youngs, D. L. 1984 Numerical simulations of turbulent mixing by Rayleigh-Taylor instability. *Physica D* **12**, 32–44.
- Youngs, D. L. 1989 Modelling turbulent mixing by Rayleigh-Taylor instability. *Physica D* **37**, 270–287.
- Youngs, D. L. 1991 Three-dimensional numerical simulations of turbulent mixing by Rayleigh-Taylor instability. *Phys. Fluids A* **3**, 1312–1320.

Youngs, D. L. 1994 Three dimensional numerical simulation of turbulent mixing by Rayleigh-Taylor instabilities.

*Las. Part. Beams* **12**, 725–750.

### Figures

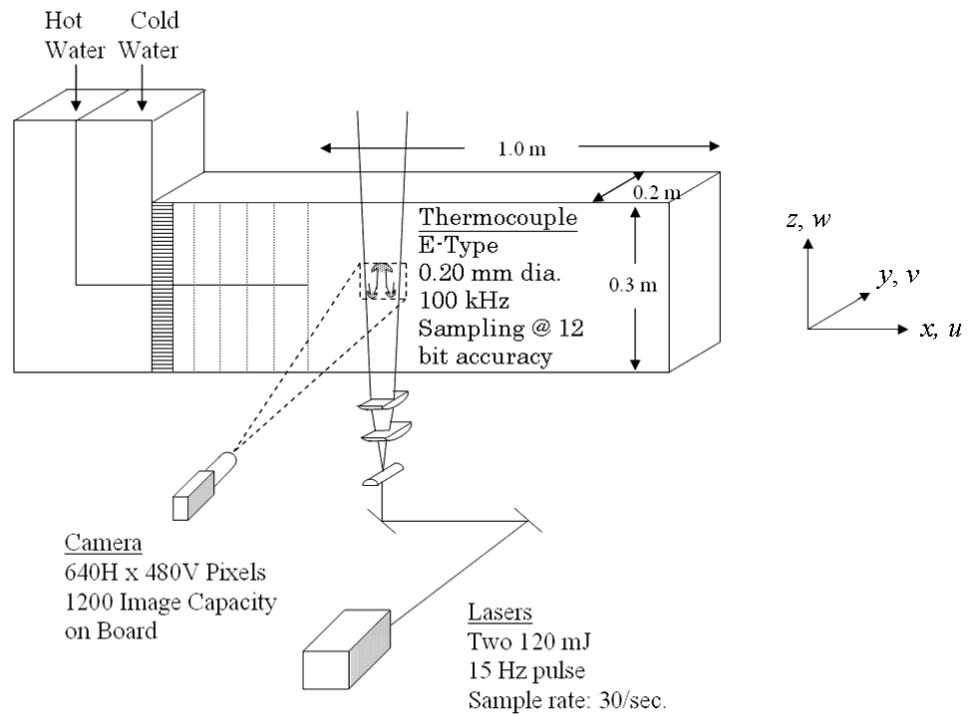


Fig. 1. Schematic of the water channel and the associated diagnostics. The conventions for the coordinates and velocities are shown on the right-hand side.



Fig. 2. Photographic image of a water channel experiment. The mean flow is from left-to-right.



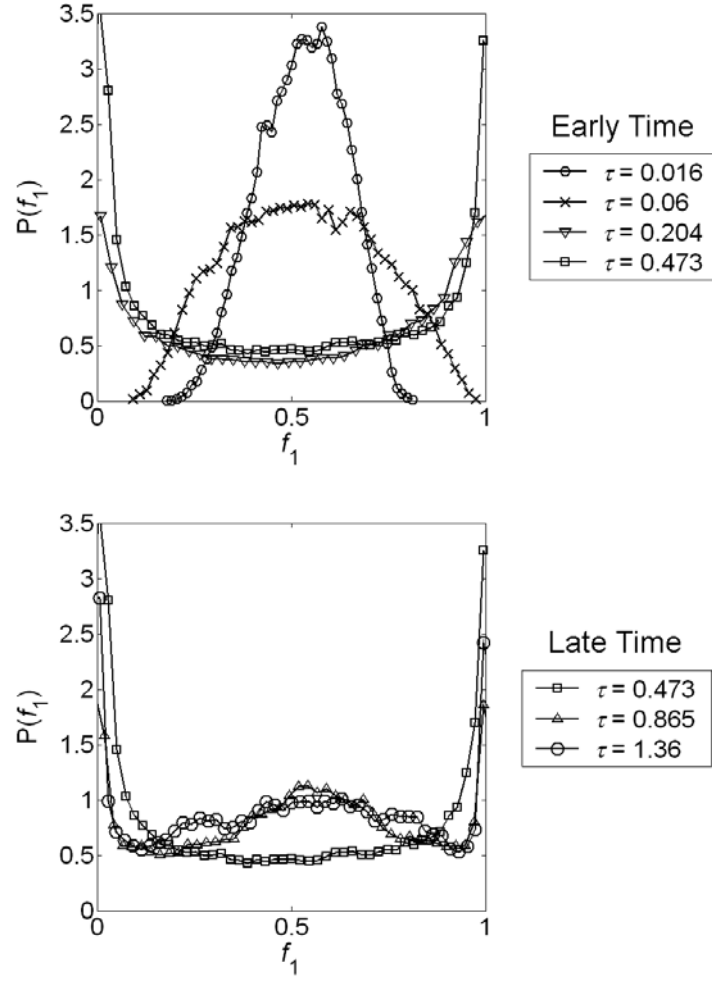


Fig. 3. Time-evolution of the early-time (top) and late-time (bottom) volume fraction PDF  $P(f_1)$  on the centerplane of the mixing layer.

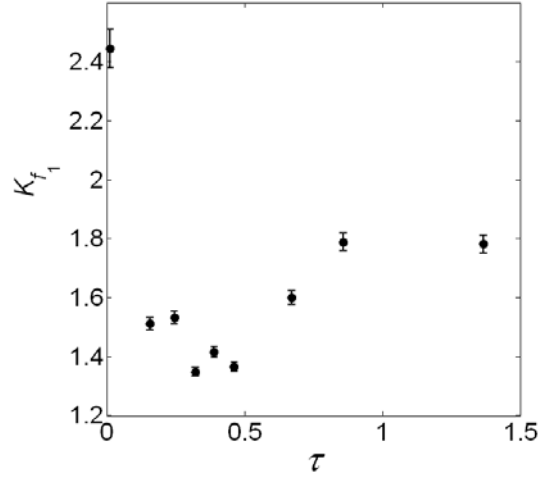


Fig 4. Time-evolution of the volume fraction kurtosis on the centerplane.

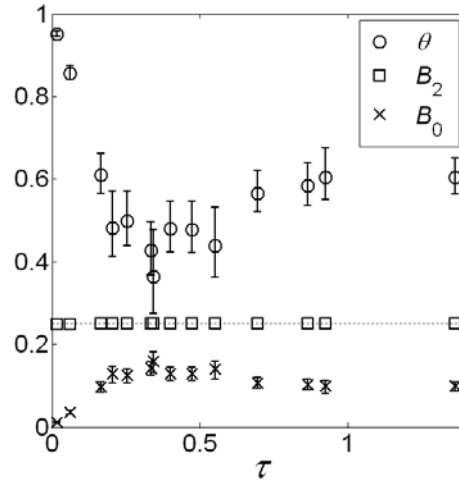


Fig. 5. Time-evolution of the molecular mixing quantities  $B_0$ ,  $B_2$ , and  $\theta$  on the centerplane. The values of  $B_2$  all approach a value of 0.25 (dotted line), indicating that all measurements reported were taken at the centerplane of the mixing layer. The error bars on the measurements are also shown.

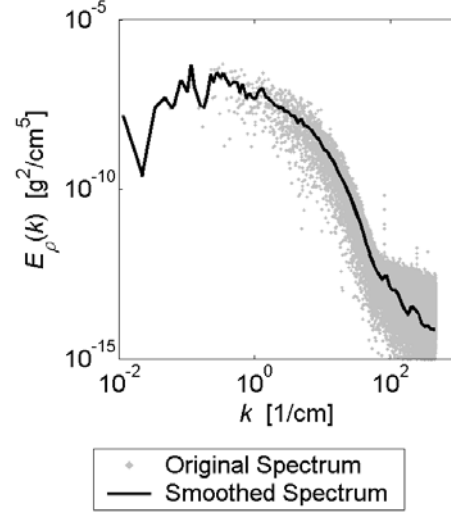


Fig. 6. Illustration of a smoothed density variance spectrum using the logarithmic binning procedure.

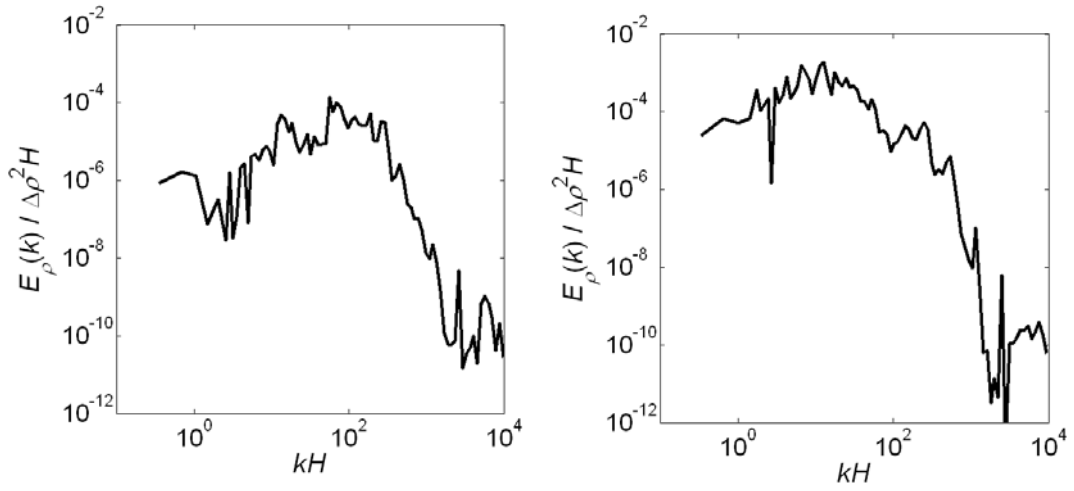


Fig. 7. The normalized density variance spectrum at  $\tau = 0.016$  or  $x = 0.5$  cm downstream (left) and at  $\tau = 0.06$  or  $x = 2.0$  cm downstream (right).

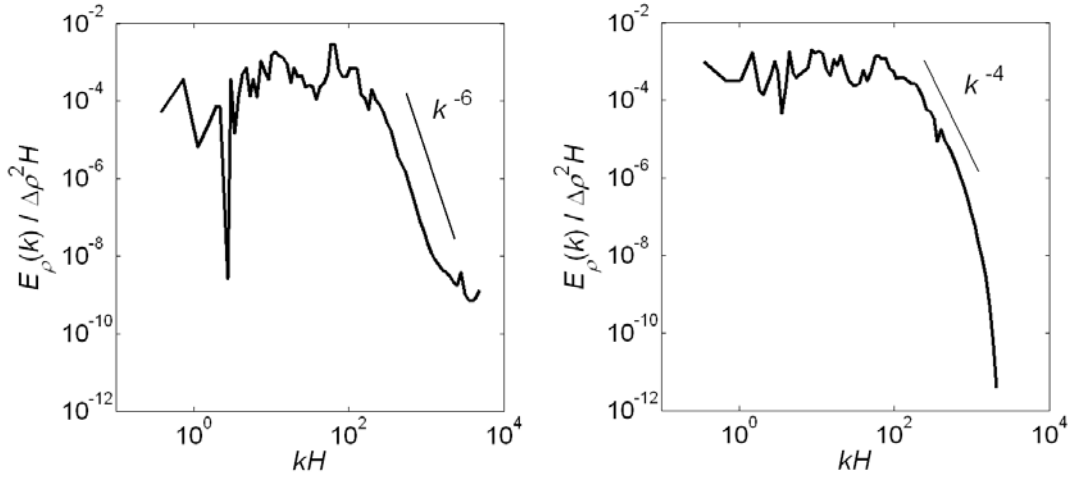


Fig. 8. The normalized density variance spectrum at  $\tau = 0.204$  or  $x = 6.0$  cm downstream (left) and at  $\tau = 0.473$  or at  $x = 15.0$  cm downstream (right).

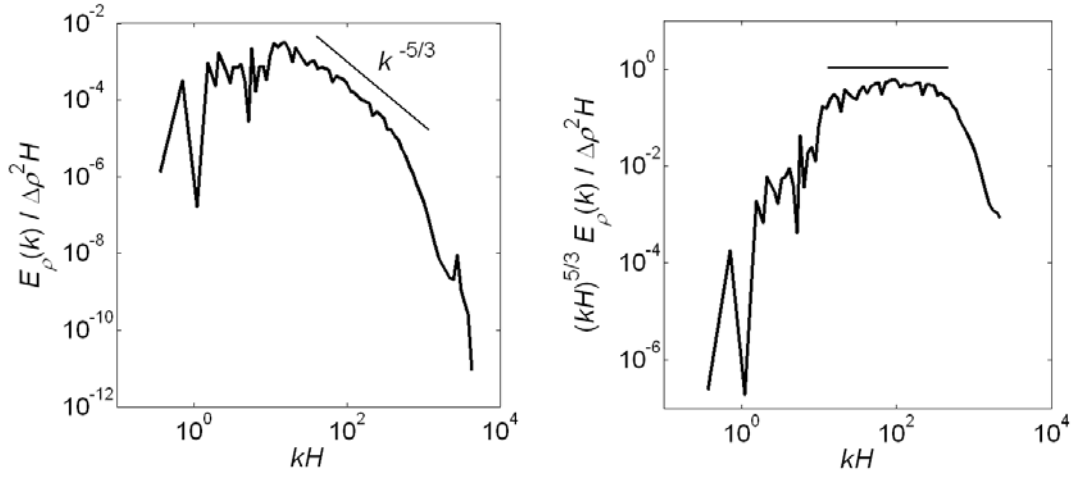


Fig. 9. The normalized density variance spectrum at  $\tau = 0.865$  or  $x = 25.0$  cm downstream (left). The compensated spectrum (right) at  $\tau = 0.865$  indicates a short range of apparent  $k^{-5/3}$  scaling.

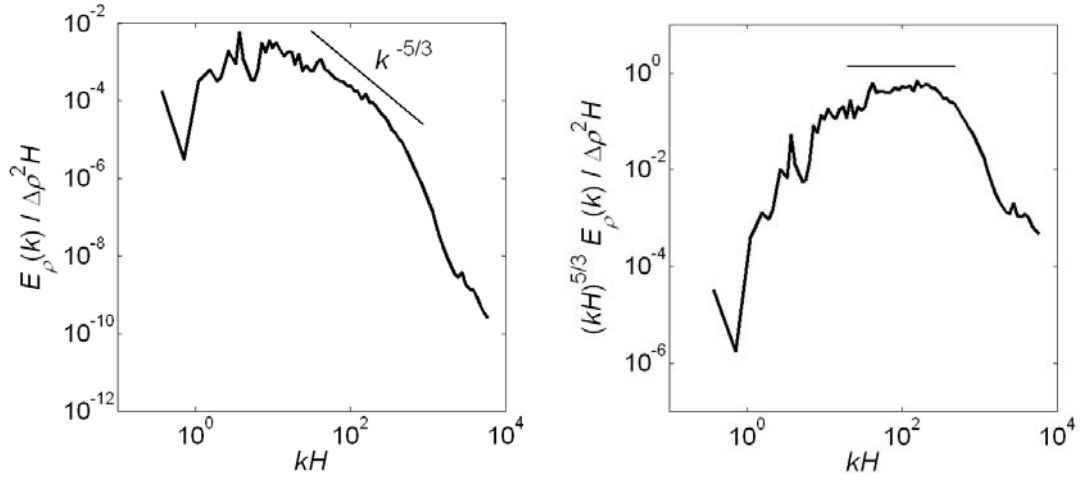


Fig. 10. The normalized density variance spectrum at  $\tau = 1.36$  or at  $x = 40.0$  cm downstream (left). The compensated spectrum (right) at  $\tau = 1.36$  indicates a short range of apparent  $k^{-5/3}$  scaling.

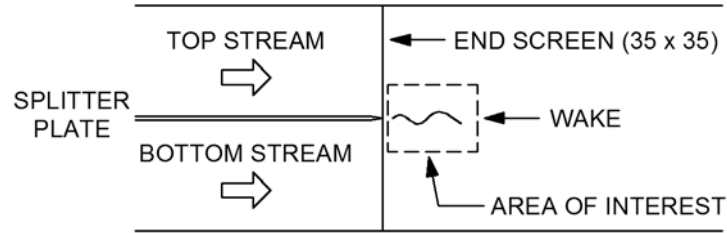


Fig. 11. Schematic of the domain measured by the PIV system in the water channel.

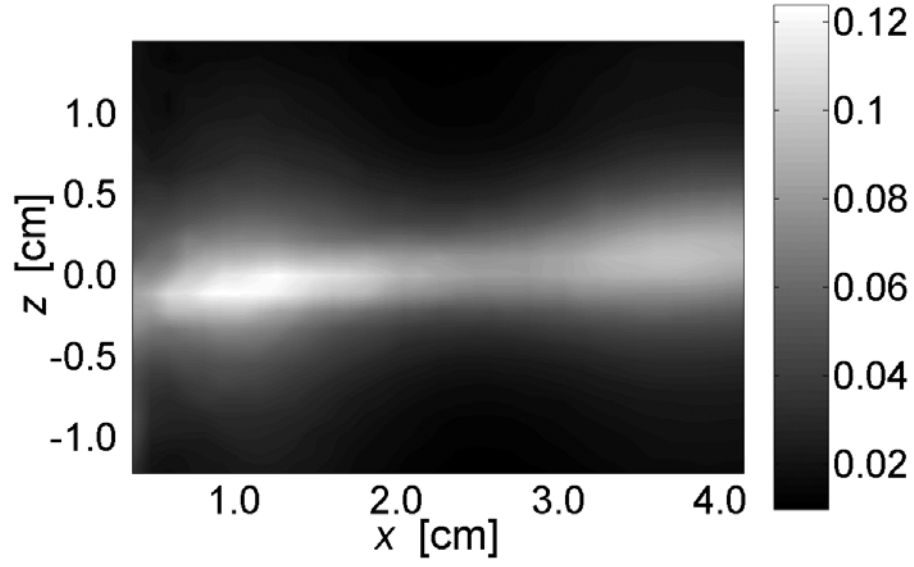


Fig. 12. Field of the vertical velocity variance  $\langle w'^2 \rangle$  at downstream locations  $x = 0.5\text{--}4.0\text{ cm}$ .

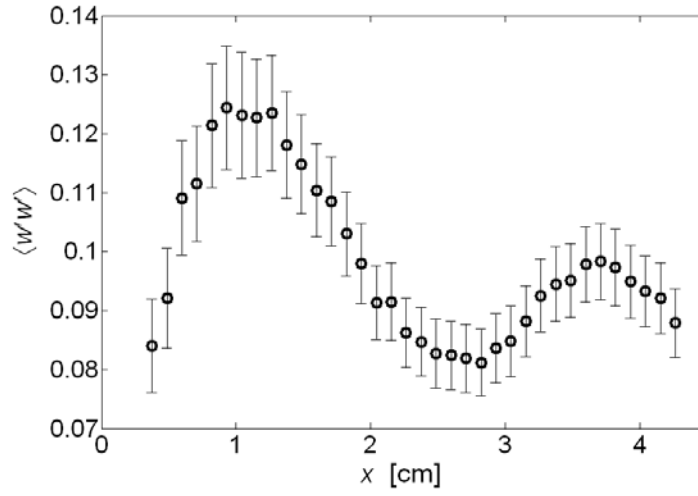


Fig. 13. Early-time decay of  $\langle w'^2 \rangle$  in the streamwise direction following the trailing edge of the splitter plate with the channel in a non-buoyant configuration. The error bars on the measurements are also shown.

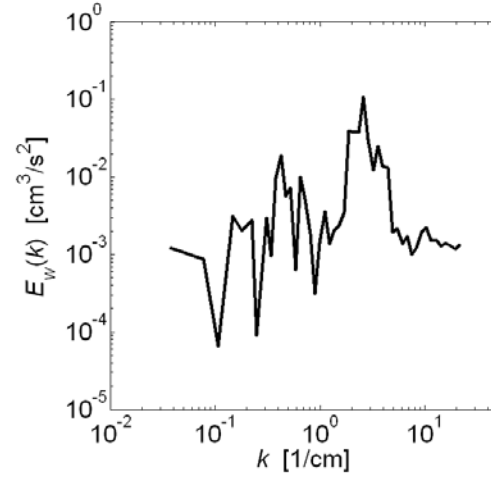


Fig. 14. The vertical velocity variance spectrum at a distance  $x = 1.0$  cm from the splitter plate.

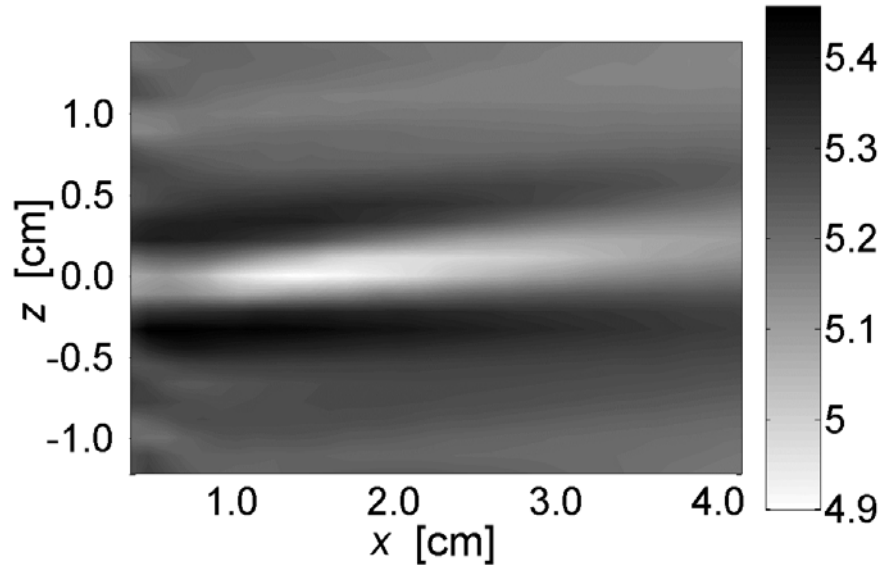


Fig. 15. Contour of the mean advective velocity  $\langle u \rangle$  in the near wake of the splitter plate with the water channel in a non-buoyant configuration.

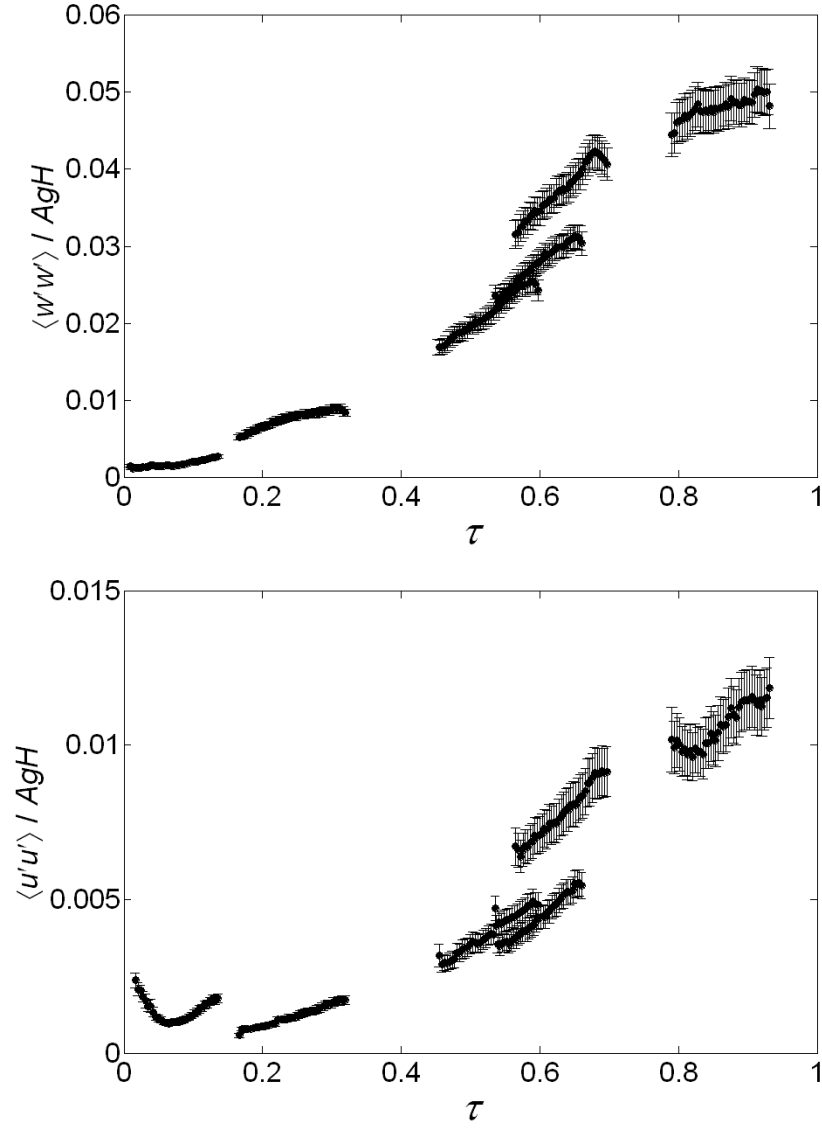


Fig. 16. Time-evolution of the vertical (top) and horizontal (bottom) velocity variance on the centerplane. The error bars on the measurements are also shown.



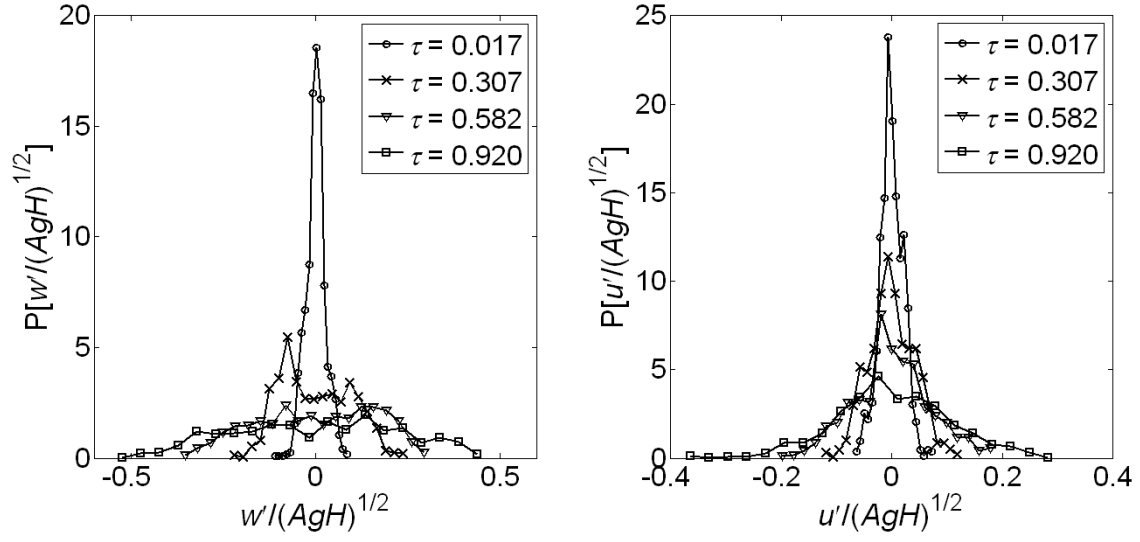


Fig. 17. Time-evolution of the PDF of the vertical (left) and the horizontal (right) velocity fluctuations on the centerplane of the mixing layer.

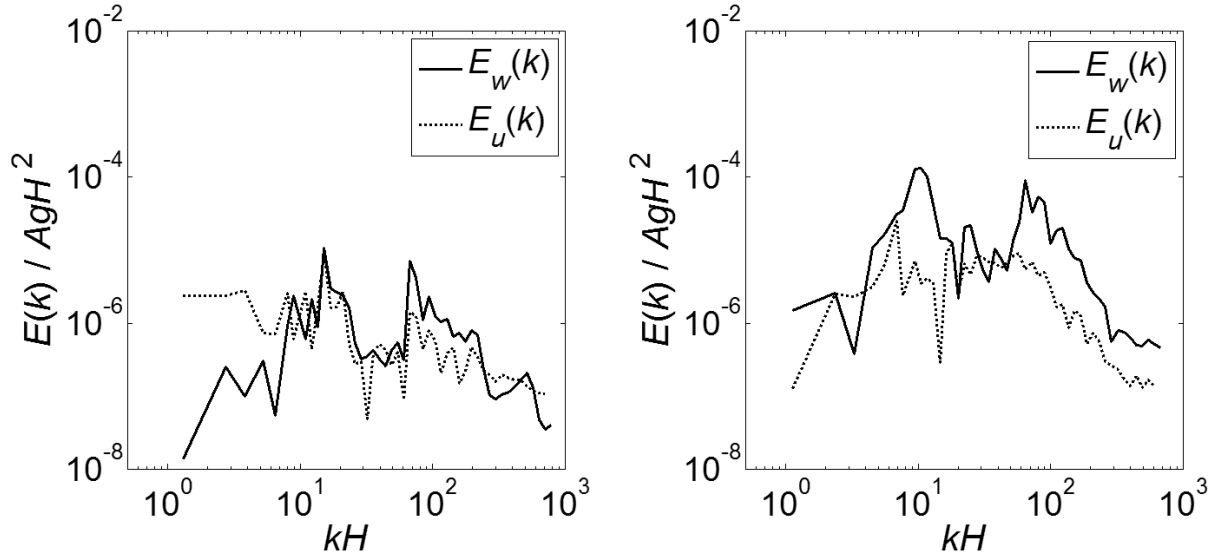


Fig. 18. The normalized vertical (solid) and streamwise (dashed) velocity variance spectrum at  $\tau = 0.017$  downstream (left) and at  $\tau = 0.307$  downstream (right).

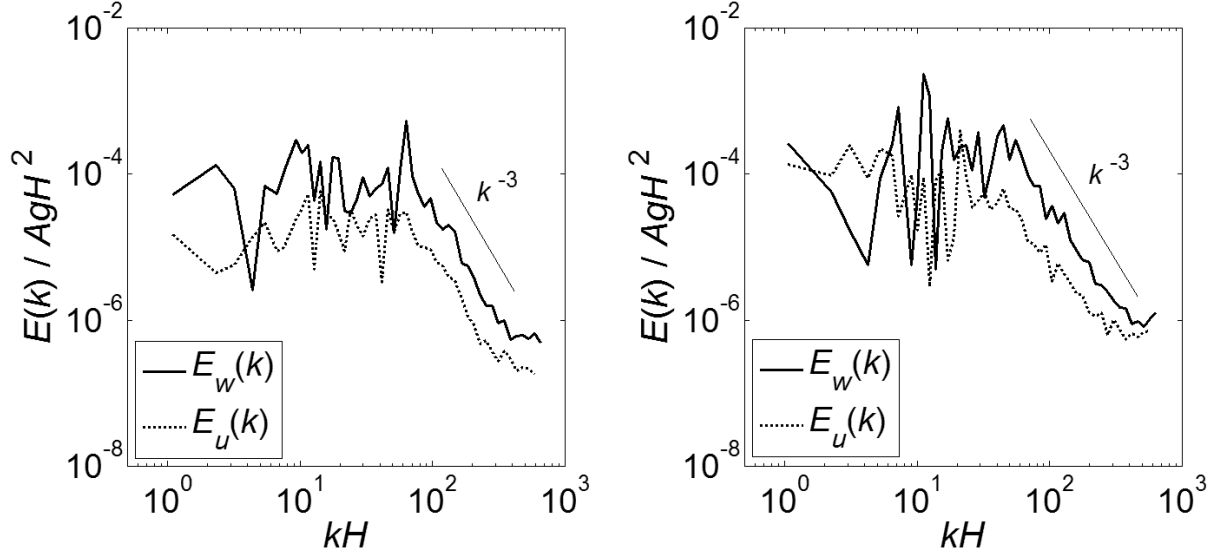


Fig. 19. The normalized vertical (solid) and streamwise (dashed) velocity variance spectrum at  $\tau = 0.582$  downstream (left) and at  $\tau = 0.920$  downstream (right).

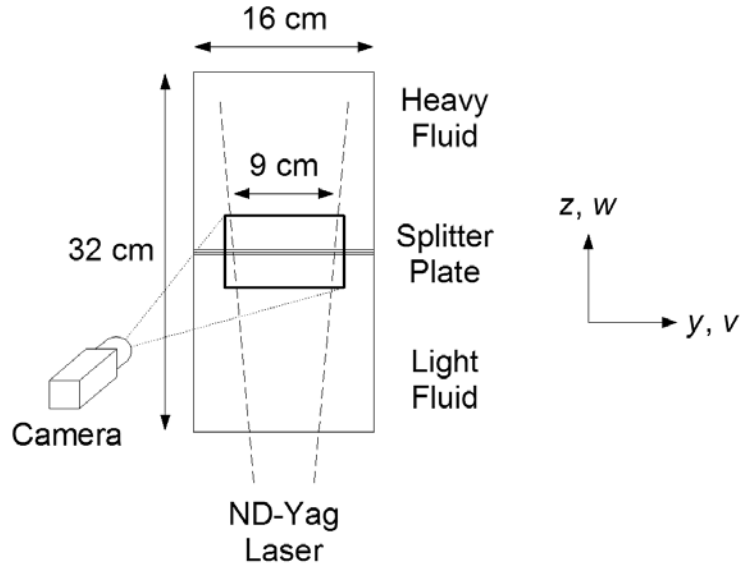


Fig. 20. Schematic of the experimental laser sheet configuration for the spanwise PLIF measurements.

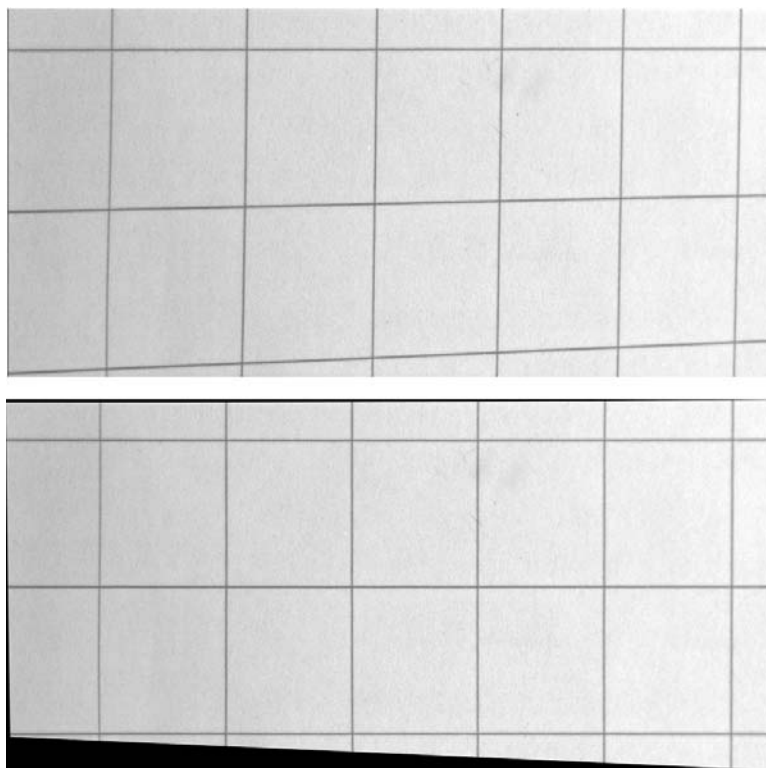


Fig. 21. Raw image of the warped calibration grid (above) and the dewarped calibration grid (below).

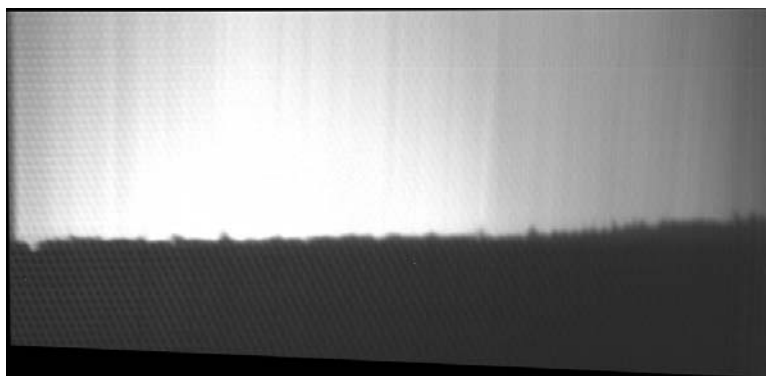


Fig. 22. PLIF image of the spanwise interfacial perturbation.

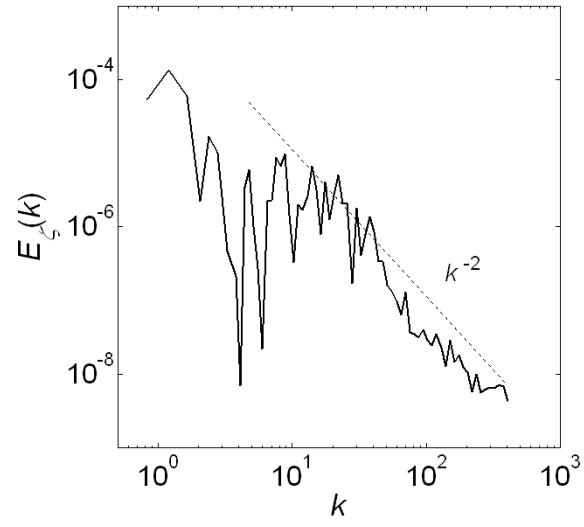


Fig. 23. The spectrum of the spanwise interfacial perturbations.

### Tables

Parameter	Value	Description
$\rho_1$	0.9986 g/cm <sup>3</sup>	density of top (cold) stream
$\rho_2$	0.9970 g/cm <sup>3</sup>	density of bottom (warm) stream
$A$	$7.5 \times 10^{-4}$	Atwood number
$U_m$	4.75 cm/s	mean velocity
$\mu_1$	0.009 g/(cm s)	dynamic viscosity of top stream
$\mu_2$	0.011 g/(cm s)	dynamic viscosity of bottom stream
$Pr$	7.0	Prandtl number $Pr \equiv \nu/D$
$H$	32.0 cm	total height of channel

Table 1. Parameters in a typical experiment.

Downstream location $x$ (cm)	Non-dimensional time $\tau$
0.5	0.016
2.0	0.061
5.0	0.166
6.0	0.204
8.0	0.255
10.0	0.342
11.3	0.334
12.5	0.400
15.0	0.473
16.0	0.552
20.1	0.694
25.0	0.865
27.0	0.924
40.0	1.363

Table 2. Downstream locations of centerplane temperature (density) measurements and the corresponding non-dimensional time.

Experiment	Physical window size (cm)	Final interrogation window (pixels)	Spatial resolution (cm)
Non-buoyant ( $A = 0$ )	$4.44 \times 3.33$	$32 \times 32$	0.22
Rayleigh-Taylor ( $A \approx 7 \times 10^{-4}$ )	$5.33 \times 4.00$	$32 \times 32$	0.27

Table 3. PIV Diagnostic parameters in a typical experiment.